Shear Velocity Model of Alaska Via Joint Inversion of Rayleigh Wave Ellipticity, Phase Velocities, and Receiver Functions Across the Alaska Transportable Array

Elizabeth M. Berg[1] (ID)**, Fan-Chi Lin[1,2]** (ID)**, Amir Allam[1]** (ID)**, Vera Schulte-Pelkum[3]** (ID)**, Kevin M. Ward[4]** (ID)**, and Weisen Shen[5]** (ID)

[1]Department of Geology and Geophysics, University of Utah, Salt Lake City, UT, USA, [2]Institute of Earth Sciences, Academia Sinica, Taipei, Taiwan, [3]Cooperative Institute for Research in Environmental Sciences and Department of Geological Sciences, University of Colorado Boulder, Boulder, CO, USA, [4]Department of Geology and Geological Engineering, South Dakota School of Mines and Technology, Rapid City, SD, USA, [5]Department of Geosciences, State University of New York at Stony Brook, Stony Brook, NY, USA
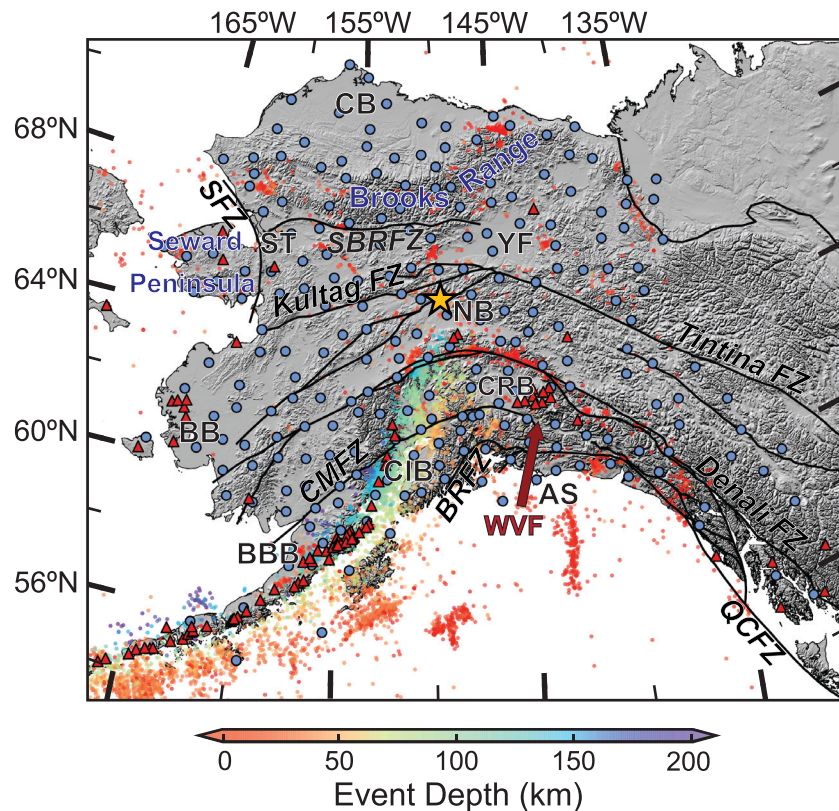
Abstract Through the Alaska Transportable Array deployment of over 200 stations, we create a 3-D tomographic model of Alaska with sensitivity ranging from the near surface (<1 km) into the upper mantle (~140 km). We perform a Markov chain Monte Carlo joint inversion of Rayleigh wave ellipticity and phase velocities, from both ambient noise and earthquake measurements, along with receiver functions to create a shear wave velocity model. We also use a follow-up phase velocity inversion to resolve interstation structure. By comparing our results to previous tomography, geology, and geophysical studies we are able to validate our findings and connect localized near-surface studies with deeper, regional models. Specifically, we are able to resolve shallow basins, including the Copper River, Cook Inlet, Yukon Flats, Nenana, and a variety of other shallower basins. Additionally, we gain insight on the interaction between the upper mantle wedge, asthenosphere, and active and nonactive volcanism along the Aleutians and Denali volcanic gap, respectively. We observe thicker crust beneath the Brooks Range and south of the Denali fault within the Wrangellia Composite Terrane and thinner crust in the Yukon Composite Terrane in interior Alaska. We also gain new perspective on the Wrangell Volcanic Field and its interaction between surrounding asthenosphere and the Yakutat Terrane.

1. Introduction

1.1. Tectonic History

Modern Alaska is a diverse geological landscape largely composed of accreted terranes with complicated active tectonics including multiple zones of subduction, arc magmatism, and a multifaceted stress regime. For simplification, the Alaskan continent can be divided into four distinct terranes separated by active right-lateral strike-slip faults. The Arctic Alaska Terrane is the northernmost of these, including the Seward Peninsula and region north of the Southern Brooks Range Fault zone (SBRFZ, see Figure 1) that was accreted in the late Jurassic (Cole et al., 1997; Plafker & Berg, 1994; Till, 2016). Between the Tintina fault and the Denali fault is the Yukon Composite Terrane, a Jurassic-aged accreted terrane thickened by repeated episodes of arc magmatism (Nokleberg et al., 1994; Plafker & Berg, 1994). Between the Denali and Border Ranges fault zone (BRFZ, Figure 1) lies the Wrangellia Composite Terrane, a Cretaceous-aged basaltic oceanic plateau and associated volcanoclastic rocks (Plafker & Berg, 1994; Trop & Ridgway, 2007). The southernmost portion of Alaska contains the Southern Margin Composite Terrane and active subduction along the entirety of the Aleutian arc. All of these terranes feature complex internal deformation histories and varying degrees of metamorphism. All Alaskan terranes (Colpron et al., 2007) are shown in Figure 2c, and major terranes are labeled.

The Arctic Alaska Terrane, including the Brooks Range, Seward Peninsula, and Colville Basin, collided with northern Laurentia in the late Jurassic, which caused significant crustal shortening of the Brooks Range and metamorphism throughout the terrane (Cole et al., 1997; Plafker & Berg, 1994; Till, 2016). In the Early
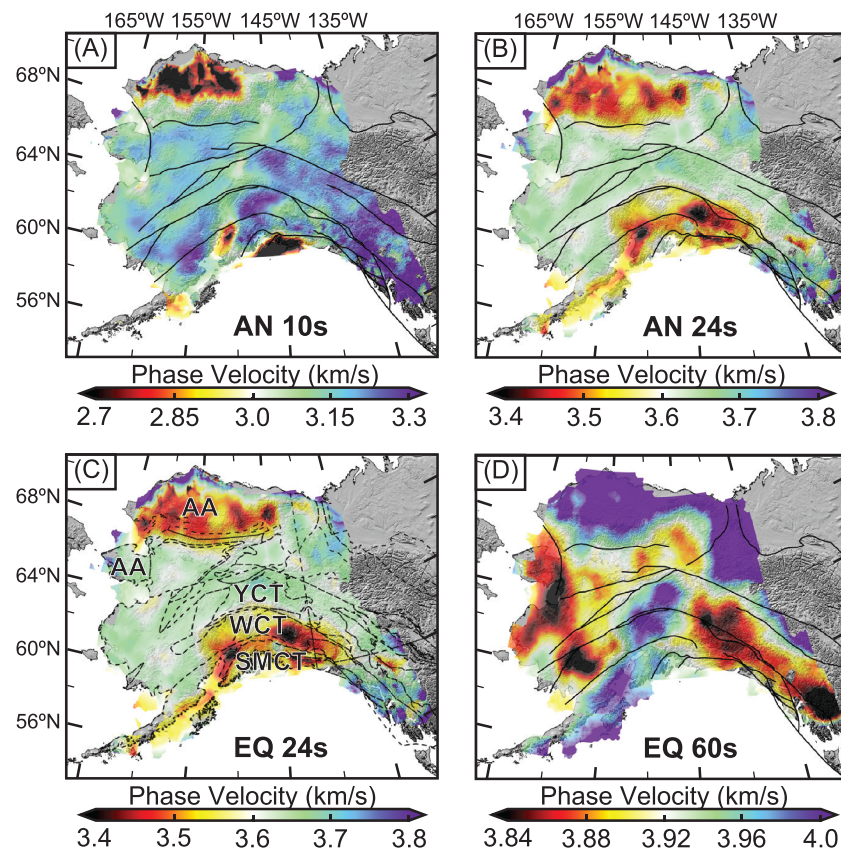
AGU
100
ADVANCING EARTH
AND SPACE SCIENCE

Journal of Geophysical Research: Solid Earth

10.1029/2019JB018582

Figure 1. Map showing topography and earthquakes from 1980 to may 2019 with $M_w > 4$, shown as colored dots according to depth. Volcanoes (Holocene and Eocene) are marked as red triangles, and Alaska transportable Array stations used for joint inversion are shown as blue circles, with I23K marked as a yellow star. Important features are labeled in the map including fault zones (skewed and ending with "FZ"), basins (bold), and the Wrangell volcanic field (red, "WVF"). Fault zones include the Sevier, southern Brooks Range, Kultag, Tintina, Denali, Castle Mountain, border ranges, and queen Charlotte fault zones. Basins include Bethel Basin, Bristol Bay basin, Colville Basin, Copper River basin, cook Inlet Basin, Alaskan shelf, Nenana Basin, Selawik trough, and Yukon flats.

Cretaceous, thickening and metamorphism continued due to the collision of the Chokotka plate (now in eastern Siberia) before the southern boundary separated in the middle Cretaceous, mostly likely due to magmatism that thermally weakened the crust, created complex crustal deformation leading to strike-slip faulting (Till, 2016), and pulled the Seward Peninsula away from the Brooks Range into its present-day position (Till et al., 1994; Till, 2016).

The Yukon Composite Terrane is primarily composed of arc magmatic rocks and more ancient continental crust that began accreting in the Early Jurassic (Nokleberg et al., 1994; Plafker & Berg, 1994). By the mid-Cretaceous, outboard trench migration (Dusel-Bacon et al., 2002) caused extension, uplift, crustal thinning, and right-lateral translation that was accommodated by the Tintina fault (Plafker & Berg, 1994). This deformation largely ended by the Paleocene, leading to the current configuration of a thin crust overlying a sharp Moho transition (Allam et al., 2017; Fuis et al., 2008; Martin-Short et al., 2018; Miller & Moresi, 2018; Ward & Lin, 2018).

The Wrangellia Composite Terrane, corresponding to the area south of the Denali fault zone and north of the Border Ranges fault zone (BRFZ), consists of island arcs, flood basalts, and volcanoclastic rocks that accreted to the Yukon Composite Terrane via northward verging subduction in the Early Cretaceous (Plafker & Berg, 1994; Trop & Ridgway, 2007). The Wrangellia Terrane has generally been deforming along northeast-southwest thrust faults since the mid-Cretaceous in addition to accumulating additional arc magmatic material (Ridgway et al., 2011). Crustal thickening within the terrane continues to the present, and the entire terrane is currently rotating counterclockwise as it is squeezed between the present-day subduction to the south and the Yukon Composite Terrane to the north (Freymueller, 2008). The Denali Fault is the main structure accommodating the rotation in central Alaska (Jadamec et al., 2013; Redfield & Fitzgerald, 1993).

Figure 2. Phase velocity maps from eikonal tomography via ambient noise (AN) at a 10 s and b 24 s periods, as well as from Helmholtz tomography via earthquake (EQ) measurements at c 24 s and d 60 s periods. Faults are shown as solid black lines, while terrane boundaries (Colpron et al., 2007) are shown as dashed black lines in (c) with terranes Arctic Alaska (AA), Yukon composite Terrane (YCT), Wrangellia composite Terrane (WCT), and southern margin composite Terrane (SMCT) labeled.

The Yakutat Terrane is a smaller feature in southern central Alaska that lies south of the Denali fault zone, between the Wrangell volcanic field (WVF) and active Aleutian arc volcanism, and overlies the Wrangellia Composite and the Southern Margin Composite Terranes. The Yakutat Terrane, young oceanic crust formed off the west coast of North America, began migrating north along the Queen Charlotte/Fairweather transform in the Eocene before subducting beneath Southern Alaska at ~35 Ma (Christeson et al., 2010; Finzel et al., 2011; Pavlis et al., 2019). The onset of Yakutat subduction corresponds to the start of Chugach and Alaska range uplift due to a decrease in the subduction angle of the Yakutat and Pacific plates; this is supported by the cessation of magmatism in the Denali volcanic gap (Finzel et al., 2011; Martin-Short et al., 2018). On the eastern edge of the subducting Yakutat Terrane, the WVF experienced northwest movement of volcanic activity ~26 to 0.2 Ma (Richter et al., 1990). Additional geochemical evidence of adakites on the southeastern edge, indicative of slab melting, and tholeiitic lavas along the central axis of the WVF, suggesting a source of partial melting of anhydrous mantle wedge material (Preece & Hart, 2004), indicate that the Yakutat Terrane directly impacted volcanism in the WVF (Eberhart-Phillips, 2006; Martin-Short et al., 2018; Richter et al., 1990).

The long history of active tectonics in Alaska has led to the formation of several major basins, including the Mesozoic foreland Colville and forearc Cook Inlet Basins, Cenozoic backarc Bristol Bay Basin, and Cenozoic stepover basins, including transtensional-transpressional Bethel Basin and rift-transtensional Copper River, Nenana, Selawik, and Yukon Flats Basins (Coleman & Cahan, 2012). These basins have been previously analyzed by geological and geophysical surveys for hazard analysis (Bruhn & Haeussler, 2006; Haeussler et al., 2000), petroleum potential (Bird, 2010; Decker et al., 1988; Kirschner, 1994; Van Kooten, 2012), and relation to tectonic processes (Cole et al., 2004; Dixit et al., 2017; Moore & Box, 2016; Plafker & Berg, 1994). Our results include the first complete 3-D tomographic maps of every major basin in Alaska with high

resolution up to the surface and throughout the entire crust. One of the main improvements of our work over previous regional tomographic efforts is the inclusion of measurements which can resolve shallow basin structure.

1.2. Previous Geophysical Imaging Studies

The implementation of the EarthScope USArray and Alaska Transportable Array (ATA) has dramatically increased the resolution of seismic imaging studies, yielding new insight into the structure and tectonic history of North America. Regional tomography results in Alaska have thus far focused on midcrustal and upper mantle structure (Jiang et al., 2018; Martin-Short et al., 2018; Ward & Lin, 2018) but have lacked resolution in the shallow crust and near surface. Other studies prior to the ATA deployment were limited by data availability and constrained to not include the entirety of Alaska (e.g., Allam et al., 2017; Eberhart-Phillips, 2006; Fuis et al., 2008; Masterlark et al., 2010), contain lower spatial resolution (e.g., Wang & Tape, 2014), or both.

Ward and Lin (2018), via joint inversion of receiver functions and ambient noise-derived Rayleigh phase velocity measurements, observed a low-velocity zone corresponding to underplated sediments beneath the Chugach mountains and variations in crustal thickness across Alaska, and provided the first direct constraint on the depth and lateral extent of the mantle wedge in Southern Alaska. Jiang et al. (2018) also used ambient noise Rayleigh wave phase velocities but additionally included earthquake-derived Rayleigh wave phase velocities and teleseismic S wave traveltimes to image the crust and upper mantle. Jiang et al. (2018) observed the Moho and mantle wedge structure previously imaged (Ward & Lin, 2018) but also achieved resolution of the upper mantle, asthenosphere, and deeper geometry of the Pacific and Yakutat slabs. Though the larger-scale features are in agreement among these newer studies, questions remain about the most complicated structures. For example, is the WVF underlain by a Wrangell slab (Jiang et al., 2018) or simply influenced by the edge of the subducted Yakutat plate (Martin-Short et al., 2018)?

Detailed tomography studies have also been performed focusing on south central Alaska (e.g., Eberhart-Phillips, 2006; Martin-Short et al., 2018; Wang & Tape, 2014; Ward, 2015). These have used earthquake and active source data (Eberhart-Phillips, 2006), earthquake Rayleigh wave phase velocities (Wang & Tape, 2014), ambient noise Rayleigh phase velocities (Ward, 2015), and joint ambient and earthquake Rayleigh phase velocities and receiver functions (Martin-Short et al., 2018). These studies determined the location of the Yakutat microplate beneath southern Alaska, potential interaction of the Pacific slab and the asthenosphere to produce Aleutian volcanism, crustal thickness variations across the Denali and SBRFZ faults, and crustal structure and influence on the WVF and provided new observations on processes responsible for the Denali volcanic gap (Eberhart-Phillips, 2006; Martin-Short et al., 2018; Wang & Tape, 2014; Ward, 2015).

Receiver function focused studies, including Miller and Moresi (2018) and Zhang et al. (2019), and refraction seismic analysis (Fuis et al., 2008) observe similar variations in crustal thickness from across the different terranes. Allam et al. (2017), through double-difference tomography, receiver functions, and fault zone head waves, observed a change in slab dip and Moho depth across the Denali fault zone and show evidence of a low-velocity anomaly in the upper mantle south of the Denali fault. Gravity and aeromagnetic surveys have also revealed similar crustal structure variations attributed to Moho depth, sediment thickness, and fold-and-thrust belts in the Brooks Range and Chugach mountains (Anderson et al., 2013; Mankhemthong et al., 2013; Saltus et al., 2006).

Our study uses Rayleigh wave ellipticity and phase velocities from both ambient noise and earthquake measurements, along with azimuthally averaged radial receiver functions, in order to constrain structure from the near surface through the crust and into the uppermost mantle. Specifically, the inclusion of Rayleigh wave ellipticity, in the form of horizontal-to-vertical (H/V) ratios, allows us to image shallower structure on a large, regional scale than prior tomography studies due to the sensitivity of H/V ratios to the uppermost crust (Berg et al., 2018; Lin et al., 2012, 2014; Tanimoto & Rivera, 2008). We perform a Markov chain Monte Carlo (MCMC) joint inversion at each ATA station (see Figure 1, blue circles) followed by a phase velocity-only deterministic inversion. This allows us to leverage the local sensitivity of receiver functions and H/V ratios while including phase velocities in the joint inversion and resolve interstation structure captured in phase velocity measurements through the follow-up inversion.

2. Data and Methods

The ATA has spanned the entire region of Alaska and westernmost Canada, a remarkable accomplishment that enables multiple studies to investigate the subsurface structure of Alaska (e.g., Jiang et al., 2018; Martin-Short et al., 2018; Miller & Moresi, 2018; Ward & Lin, 2018; Zhang et al., 2019). This study focuses on joint inversion of seismic data obtained through ambient noise and earthquakes, including Rayleigh wave ellipticity, phase velocities, and receiver functions. We use data from 231 ATA stations (Figure 1) initially deployed in southern Alaska and extending northward to encompass the entire region from June 2014 to July 2018. In addition, we supplement these data with noise cross correlations from Ward and Lin (2018), which included nearly 200 more stations mainly from previous regional-scale experiments (Ward, 2015), to obtain Rayleigh wave phase velocity maps for periods of 8–30 s in order to procure the highest resolution possible in our final inversion.

Both surface wave and receiver function analyses applied in this study have been established by previous studies (Ligorría & Ammon, 1999; Lin et al., 2009; Lin et al., 2012; Lin et al., 2014; Lin & Ritzwoller, 2011; Schulte-Pelkum & Mahan, 2014a, 2014b; Shen et al., 2012), and we only briefly summarize the processes below. Ambient noise preprocessing and cross correlation is taken from Ward and Lin (2018). We preserve relative amplitudes throughout processing so that amplitude measurements, in the form of H/V ratios, are possible (Berg et al., 2018; Lin et al., 2014). We then perform frequency-time analysis (FTAN) of the nine-component symmetric cross correlations (Bensen et al., 2007) and only retain station pairs with signal-to-noise ratios >8 and interstation distances >3 wavelengths to use in eikonal tomography and H/V ratio processing.

2.1. Phase Velocities Via Eikonal and Helmholtz Tomography

Phase velocity dispersions are sensitive to 3-D subsurface structure. We use FTAN phase traveltime information of the vertical-vertical (ZZ) noise cross correlations to obtain isotropic Rayleigh wave phase velocity maps over the periods of 8 to 30 s through eikonal tomography, as described in Lin et al. (2009). For each virtual source and period, we first fit a phase traveltime map across a 0.2° (longitude) by 0.1° (latitude) grid using traveltimes of all available virtual receivers and then derive a phase velocity map from each virtual source by solving the eikonal equation. For each grid location and period, we determine phase velocity from the average of results from every virtual source and use the standard deviation of the mean to estimate uncertainty. The final phase velocity maps (e.g., Figures 2a and 2b) are generally consistent with previous results, based on straight ray inversion (Martin-Short et al., 2018; Ward, 2015; Ward & Lin, 2018).

To obtain longer-period phase velocity maps, sensitive to deeper structure in the crust and upper mantle, we perform Helmholtz tomography (Lin & Ritzwoller, 2011) across the 231 stations of the ATA. We analyze waveforms from ~650 teleseismic events with magnitudes larger than 5 that occurred between January 2015 and August 2018. In addition to phase traveltime measurements, Helmholtz tomography uses amplitude measurements to correct for the finite frequency effect (e.g., wavefront healing) and obtain more accurate phase velocity maps. We resolve phase velocities and uncertainties from periods 24–100 s (Figures 2c and 2d), also on a 0.2°-by-0.1° grid. It is immediately apparent that the overlapping 24 s period earthquake (Figure 2c) and ambient noise (Figure 2b) phase velocity results are noticeably similar providing confidence in both sets of results.

2.2. H/V Ratios

By using Rayleigh waves extracted from noise cross correlations and from teleseisms, we are able to determine Rayleigh wave ellipticity, or horizontal-to-vertical (H/V) amplitude ratios. These measurements are sensitive to near-surface structure at each station's location, where, in essence, contrasts of soft sediments over bedrock generate high H/V ratios (e.g., sedimentary basins) and areas without a strong contrast will create low H/V ratios (e.g., crystalline rock) (Lin et al., 2012).

We determine H/V from measurements of the maximum amplitudes of the envelopes for the symmetric ZZ, ZR, RZ, and RR cross correlations obtained through FTAN, similar to and as discussed in previous studies (Berg et al., 2018; Lin et al., 2008; Lin et al., 2012; Shen et al., 2012). Here Z and R represent vertical and radial components, while the first and second indices represent the component at the source and receiver station of the cross correlation, respectively. H/V at each source station is measured from RZ/ZZ and RR/ZR, and the receiver station through ZR/ZZ and RR/RZ. We retain robust measurements on the 231

ATA stations from 8–30 s periods by imposing rotation and excitation criteria (Lin et al., 2008; Lin et al., 2014). Applying rotation criteria guarantees a retrograde Rayleigh wave is being measured. After applying as-needed 2-π jump corrections and taking arrival time shifts between radial and vertical sources versus receivers into account, rotation criteria enforce that phase traveltime differences between the four components (ZZ, ZR, RZ, and RR) are no larger than one fourth of the period. For a Rayleigh wave, a radial force arrives one fourth of a period (a 90° phase shift) later than a vertical source, and a radial receiver will observe arrivals one fourth of a period earlier than a Rayleigh wave observed on the vertical component. Excitation criteria, on the other hand, remove measurements that have greater than 25% difference between the ratios of RZ/ZZ and RR/ZR for the source station or ZR/ZZ and RR/RZ for the receiver. This ensures that the Rayleigh wave ellipticity measurement is consistent across both radial and vertical excitations.

For each station and period, we average all H/V measurements, including the station acting as source or receiver, that satisfies the selection criteria to obtain the final H/V ratio. We estimate uncertainty from each station's standard deviation of the mean. These final H/V ratios from ambient noise cross correlations are shown in Figures 3a and 3b for periods of 10 and 24 s, respectively. The individual station measurements are shown as circles shaded according to H/V ratio value, and the underlying map is created via Gaussian smoothing of these measurements to better distinguish connections to known geologic and tectonic features. For longer periods, we use teleseismic Rayleigh waves to constrain the H/V ratios (Lin et al., 2012). Using the events previously described in obtaining phase velocity Helmholtz tomography, we are able to obtain H/V ratios from 24–100 s and show maps of H/V at 24 and 60 s periods in Figures 3c and 3d. Similarities from the earthquake-derived (Figure 3c) and the ambient noise-derived H/V ratios at 24 s period (Figure 3b) are significant, providing confidence in our methods and measurements.
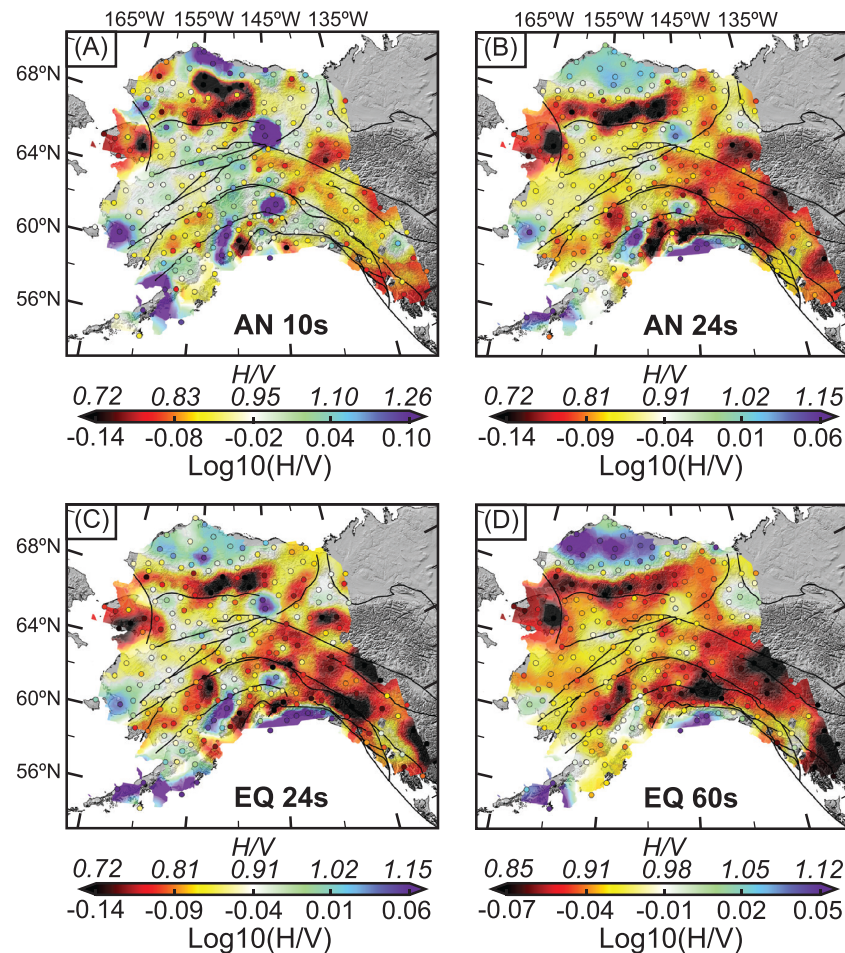
2.3. Receiver Functions

We include receiver functions in our study in order to obtain additional constraints on the layered, horizontal interface structure beneath each station (Allam et al., 2017; Langston, 1979; Park & Levin, 2016; Shen et al., 2016; Ward & Lin, 2018). Receiver functions resolve subsurface P to S conversions due to structural contrasts from teleseisms by deconvolution (Langston, 1977; Vinnik, 1977; Ligorria & Ammon, 1999). In this study we use receiver functions on 231 ATA stations created for P and P_{diff} arrivals and their coda from all events between June 2014 and July 2018 with $M_w > 5.0$ and epicentral distances 28° to 150° through the time domain iterative method of Ligorria and Ammon (1999). We use a relatively high upper frequency cutoff in the deconvolution (Gaussian filter factor 3, corresponding to a pulse length of ~1 s) to match the intracrustal resolution capability of the surface wave data.

Receiver function analysis alone is susceptible to interference from shallow interface (e.g., basin) reverberations that can impact deeper interface arrivals (Yeck et al., 2013), back azimuth dependence (Schulte-Pelkum & Mahan, 2014a, 2014b), and uneven sampling related to azimuthal distribution of seismicity (Allam et al., 2017). In order to ensure stable deconvolutions and robust results, receiver functions are initially chosen via an automated process (Schulte-Pelkum & Mahan, 2014a), with minimum signal-to-noise ratio criteria on the raw vertical component, variance reduction of the deconvolved time series, and amplitude and pulse length requirements. Radial receiver function arrival times as well as conversion amplitudes depend on slowness, and we apply corrections for both to a standard ray parameter of 0.06 s/km (Schulte-Pelkum & Mahan, 2014a). The resulting receiver functions are binned by back azimuth to remove the dominance of back azimuths with high seismicity. To remove azimuthal variations due to converter dip, horizontal scattering, and anisotropy, we calculate the azimuthal bin average over all back azimuth bins, obtaining a single average radial receiver function per station that represents predominantly the 1-D isotropic structure under the station (Schulte-Pelkum & Mahan, 2014a, 2014b).

2.4. Two-Part Inversion

As Rayleigh wave phase velocities, H/V ratios, and receiver functions distinguish varying attributes of 3-D Earth structure due to the differing sensitivity of each type of measurement, in this study we perform a two-step inversion process (e.g., Ward et al., 2014). The first step consists of a nonlinear piecewise 1-D Bayesian MCMC joint inversion of the receiver function, H/V ratios, and phase velocities, from Eikonal and Helmholtz tomography, determined at each station location (Shen & Ritzwoller, 2016). We note that the phase velocities are from the grid point corresponding to each station's location. The second step,

Figure 3. H/V maps via ambient noise cross correlations (AN) at a 10 s and b 24 s periods, as well as from earthquake measurements at c 24 s and d 60 s periods. Circles indicate station measurements, and the underlying smoothed map is shown to assist illustration of overall features observed at individual stations, including higher H/V ratios in sedimentary basins (e.g., Yukon flats, and cook inlet) and lower H/V ratios in areas of crystalline rock (e.g., Brooks Range).

utilizing the smoothed model from the first step as the starting model, consists of a deterministic inversion of phase velocities at all grid points and not limited to only station locations. Due to the complexity within Alaska and the station-localized sensitivity of H/V ratios and receiver functions, the 1-D structure at each station is imaged before resolving structure between stations across 3-D volume, where interstation phase velocity measurements are most sensitive. This two-step inversion approach allows us to obtain 1-D models and their associated uncertainties at all station locations and a 3-D model on regular grid points.

2.4.1. MCMC Joint Inversion

The initial Bayesian MCMC inversion benefits from full exploration of the parameter space and is unlikely to be trapped in a local minimum while simultaneously quantifying model uncertainty (Roy & Romanowicz, 2017; Shen et al., 2012). The MCMC model space of our study consists of three layers from the surface to a total depth of 145 km, including a top linear sedimentary layer, a crustal layer described by four cubic B-splines, and a mantle layer described by five cubic B-splines, a total of 13 free parameters (see Table 1). The starting model for each station in this study is derived from the global diffraction model of Shapiro and Ritzwoller (2002), where the thickness of the top layer is defined from the maximum V_s gradient in the top 15 km, and the thickness of the crust is derived from the maximum V_s gradient below 20 km depth. At each station, the a priori consists of Gaussian probability distributions centered around the starting model parameters and empirically chosen widths to provide full sampling of model space. The a priori distribution for the crustal thickness (Moho depth) is presented as a histogram in Figure 4h at Station I23K near Minto, Alaska, on the northern edge of the Nenana Basin, denoted as a yellow star in Figure 1.

Table 1
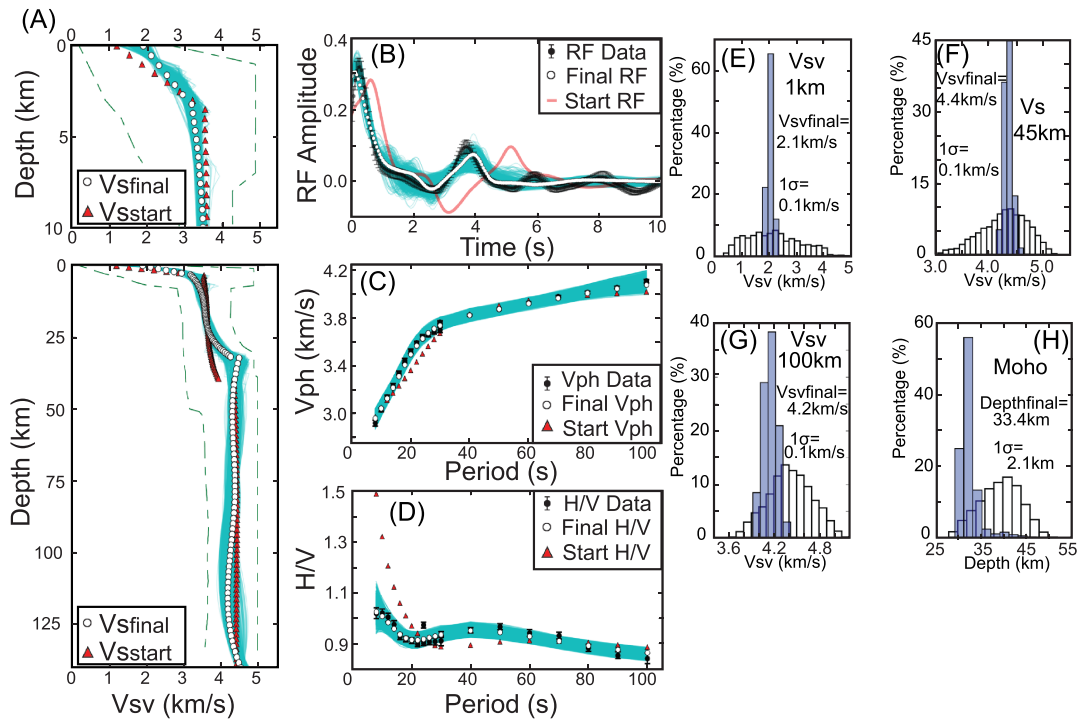*Prior Distributions in Joint Inversion*

Parameters	Range	Gaussian width
Sedimentary layer thickness	$m_0 \pm m_0$ (km)	0.1 (km)
Sedimentary layer Vsv (top and bottom)	$m_0 \pm 1.5$ (km/s)	0.05 (km/s)
Crustal thickness	$m_0 \pm 0.2\, m_0$ (km)	1.0 (km)
Crust b-spline coefficients (4 total)	$m_0 \pm 0.2\, m_0$ (km/s)	0.05 (km/s)
Mantle b-spline coefficients (5 total)	$m_0 \pm 0.2\, m_0$ (km/s)	0.05 (km/s)

Note. All 13 parameters (left) listed, (middle) the ranges explored with m_0 corresponding to the starting model variable's associated value, and (right) the Gaussian half-width used to define the a priori distributions.

We follow the procedure described by Shen et al. (2012) and Berg et al. (2018) to determine posterior distributions from the prior distributions, with minor adjustments. Specifically, we only include a loose constraint of maximum Vs in the crust of 4.9 km/s in order to allow complex structure to be better resolved. We do not require a positive Vs jump between the top linear layer and the crustal layer, but we do require a positive jump between the bottom of the crustal layer and the top of the mantle layer to better stabilize our result and estimation of the Moho. Models are randomly selected from the a priori distribution by simultaneously perturbing all 13 parameters. Model misfit and the probability of acceptance defined by the likelihood function and Metropolis law (Shen et al., 2012) dictate whether to accept a new perturbation from this model or to return to the previous one. This prevents the inversion from becoming trapped in a local minimum (Berg et al., 2018; Shen et al., 2012, 2016). Model misfit is determined from the square root of the χ^2 difference between observed and forward calculated phase velocities, H/V ratios, and receiver functions for that station (Herrmann & Ammon, 2004; Shen et al., 2012), weighted by 20%, 40%, and 40% for each data set, respectively. This weighting allows maximization of the H/V ratios and receiver functions, which are sensitive to near-station structure, while still taking phase velocity information into consideration. Note that in the MCMC inversion, uncertainties of phase velocities and H/V ratios are scaled up by 1.5 of the standard deviation of each mean measurement to account for potential systematic bias not encompassed by measurement variation (Lin et al., 2009; Lin et al., 2012).

We require a minimum number of 500 models in the posterior, defined by all models with misfit less than 1.5 of the absolute lowest model's minimum misfit. While our estimation of posterior distribution is efficient and removes models accepted prior to reaching the equilibrium state, this also effectively trims our posterior distribution, and we acknowledge potentially underestimating true posterior distribution width. All MCMC inversions begin with 3,000 randomly generated iterations from the original starting model. We repeat this process, or jump, from the starting model 12 times. If the posterior does not contain more than 500 models, or the minimum misfit model is too large ($\chi > 1.2$), we increase the number of iterations and jumps by factors of 4 and 1.5, respectively. If we are still unable to fit the data, we increase the space searched by doubling the width of the a priori distribution (e.g., 20% B-spline and crustal thickness a priori distribution becomes 40% B-spline a priori distribution). At this stage, if data misfit is still poor (χ-misfit >2), or if the posterior is near the edge of the model space, we use the final model from the previous MCMC inversion attempt as a starting model and rerun the MCMC inversion, in essence shifting the a priori distribution to better enable finding a best fit model. Many stations (50% of all stations) require the rerun of the MCMC inversion to best fit the data within given model space. The number of accepted models in the posterior is on average larger than 2,000. Through this process, we aim to retain computational efficiency while also avoiding potential biases in our results.

At the end of the MCMC inversion, we choose the minimum misfit model as the final model and use the posterior distribution to estimate the model's uncertainty. Figure 4 demonstrates the MCMC inversion process for Station I23K. In Figure 4a the starting model is shown as red triangles, the a priori distribution as green dashed lines, posterior models (1,750 models for this station) as light blue strands, and the minimum misfit model as white dots. Figures 4b–4d contain the forward models determined from each Vs model in Figure 4a for receiver functions, phase velocities, and H/V ratios, respectively. Clear misfit improvement is observed for the posterior models compared to the starting model. The a priori and posterior distributions are shown in Figures 4e–4h for multiple depths as well as the Moho depth parameter. The narrow distributions of the
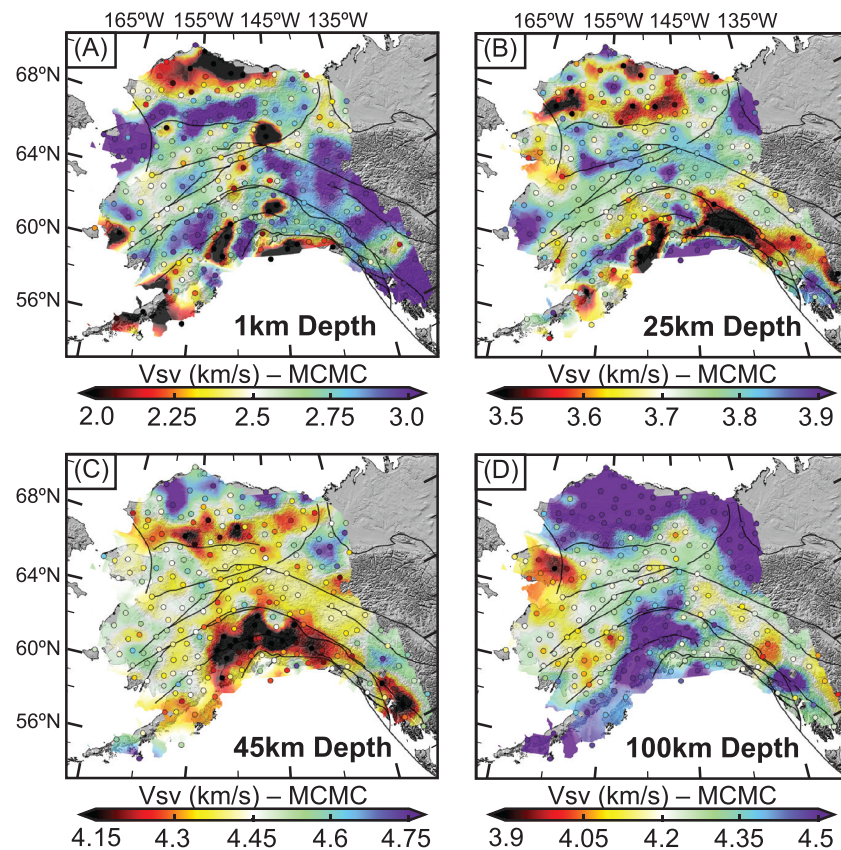
Figure 4. Markov chain Monte Carlo result for station I23K (yellow star, Figure 1), on the edge of the Nenana Basin. A overall search area (green dashed lines), posterior models (cyan lines), starting model (red triangles), and final minimum misfit model (white circles). (b–d) the starting model's forward result of data (red triangles or red line), data (error bars and black dots), posterior models' forward results (cyan lines), and final model's result (white circles) for a given receiver function, phase velocity data, and H/V ratio data. (e–h) the narrow Gaussian distribution of results within the posterior compared to the allowed search area. The mean, final minimum misfit model value, and standard deviation are denoted for each.

posterior and overall strong fit to the data demonstrate the sensitivity of the data to subsurface shear velocity structure. In order to show the impact of H/V ratios on the width of the posterior distribution at shallow depths, we have included the result of an MCMC joint inversion using only phase velocity and receiver function data at I23K in supporting information Figure S1. The final MCMC shear velocity model of the region is shown at depths of 1, 25, 45, and 100 km at each station, as well as the Gaussian-smoothed result as an underlying map, in Figure 5. We also include maps at these depths of the standard deviation of the posterior to demonstrate the certainty of our MCMC results (see Figure 6). We note that our model's lateral resolution is strongly controlled by interstation distance and is expected to be similar to previous USArray studies (Lin et al., 2009; Shen & Ritzwoller, 2016). We determine Vp and density structure in our inversion for the top linear and crustal layers from the empirical relations described in Brocher (2005). We determine Vp and density for the upper mantle as described in Shen and Ritzwoller (2016). Specifically, density in the upper mantle is scaled from Vs perturbations relative to 4.5 km/s with 10 kg/m^3 per 1% velocity change (Hacker & Abers, 2004). Vp/Vs ratio in the upper mantle is set to be 1.789 as suggested for AK135 (Shen & Ritzwoller, 2016). While further model and misfit improvement can in principle be achieved by introducing additional free parameters, the focus of this study is to obtain a robust shear velocity model.

2.4.2. Phase Velocity-Only Inversion

The second part of our inversion processing includes a phase velocity-only deterministic inversion of phase velocities from Eikonal and Helmholtz tomography to better resolve variation of interstation lateral structure while retaining the main depth structure variation already constrained by the MCMC inversion. Based on the 1-D shear velocity from MCMC inversion at each station (Figure 5), we first determine reference shear velocities from the surface to 145 km depth in 0.5 km depth increments over a 0.2° (longitude) × 0.1° (latitude) grid through narrow Gaussian smoothing, where the Gaussian width is the distance to the nearest three stations. We use this smoothed result as a starting model (underlying maps in Figure 5) for each grid point to perform a deterministic damped phase velocity-only inversion (Herrmann & Ammon, 2004) using the

AGU
100
ADVANCING EARTH
AND SPACE SCIENCE

Journal of Geophysical Research: Solid Earth

10.1029/2019JB018582

Figure 5. Shear velocity (km/s) result from MCMC joint inversion at all ATA stations at (a) 1 km, (b) 25 km, (c), 45 km, and (d) 100 km depths. Actual value is shown as a circle, and underlying map is the Gaussian-smoothed result from all stations. Note that the smoothed model is used as the starting model in the final phase velocity-only inversion.
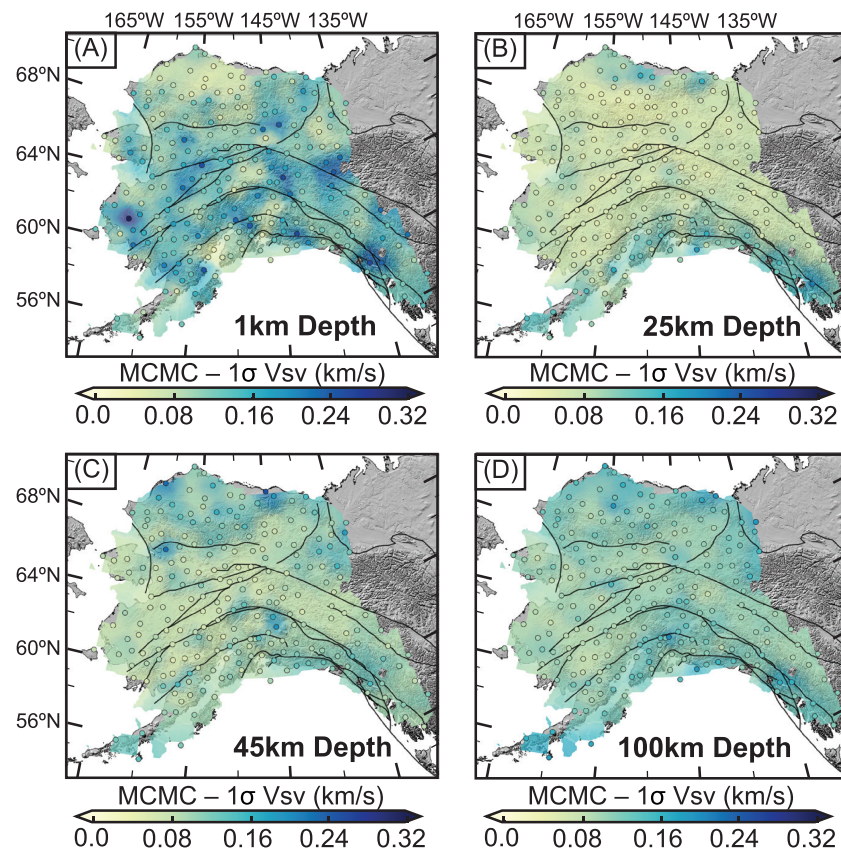
phase velocities previously determined from Eikonal and Helmholtz tomography to obtain the final 3-D shear velocity model. The inversion is allowed to iterate up to 50 times but is terminated when the misfit to the phase velocity data does not improve by 1% over the previous iteration. The mean number of iterations is ~15 and decreases phase velocity χ misfit from 2.2 over the whole grid to 0.8. Overall, some minor but noticeable differences between the MCMC velocity model (Figure 5) and the final model (Figure 7) are observed where the result from the final phase velocity-only inversion tends to be more smoothed due to decreased impact of erroneous/enigmatic single station measurements. We note that no change is observed for the 1 km depth map, which is somewhat expected as Rayleigh wave phase velocities above 8 s period have limited sensitivity to uppermost crustal structure (Lin et al., 2012).

3. Results

3.1. H/V and Phase Velocity Results

Figures 2a and 2b show phase velocity maps derived from eikonal tomography using ambient noise cross correlations. From the 10 s period phase velocity map, shown in Figure 2a and mainly sensitive to depths of ~10–15 km in the upper crust, we observe lower phase velocities in the Colville Basin, Cook Inlet, and Alaskan Shelf and higher phase velocities in the Chugach Range, Brooks Range, Seward Peninsula, and near the Mackenzie Mountains. From the 24 s period phase velocity map (Figure 2b), mostly sensitive to 30–40 km depth in the lower crust and uppermost mantle, we observe slower phase velocities south of the Denali fault and north of the Brooks Range and faster phase velocities in the interior of Alaska. This 24 s period result likely reflects crustal thickness variations similar to previous studies, with thicker crust south of the Denali fault and north of the SBRFZ (Allam et al., 2017; Fuis et al., 2008; Jiang et al., 2018; Martin-Short et al., 2018; Miller & Moresi, 2018; Ward & Lin, 2018).
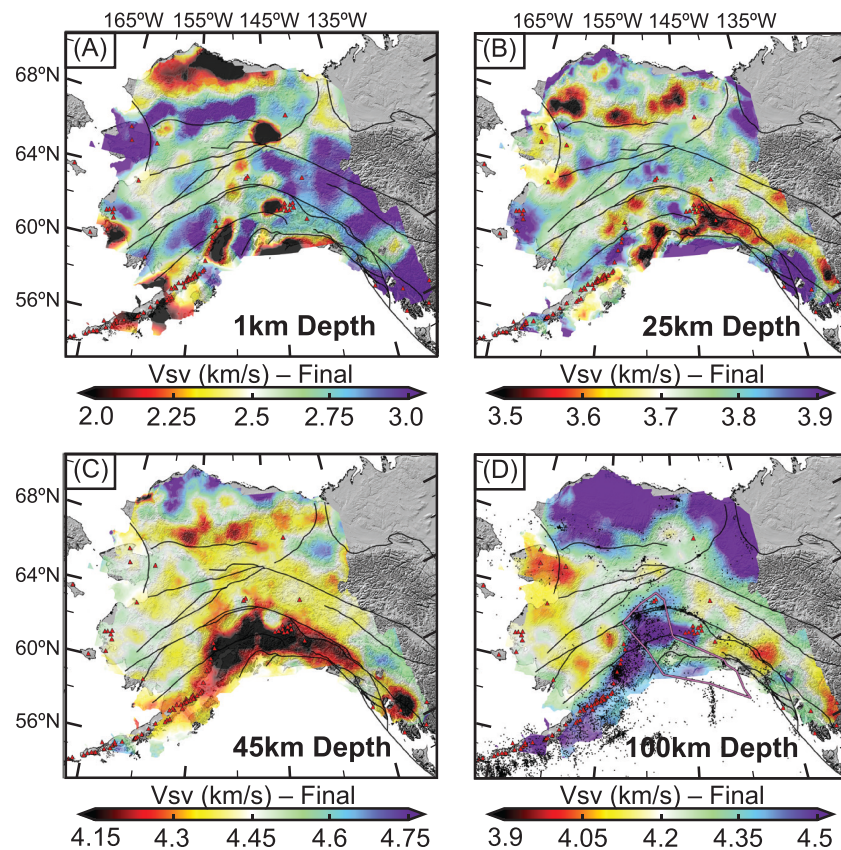
Figure 6. Standard deviation of posterior distribution of (a) 1 km, (b) 25 km, (c) 45 km, and (d) 100 km depths shows certainty and sensitivity of MCMC results to subsurface structure.

Phase velocities obtained from earthquake Rayleigh waves through Helmholtz tomography are shown at 24 and 60 s periods in Figures 2c and 2d, respectively. The similarities between Figures 2c and 2b, including low phase velocities in the north and south while higher phase velocities are in the interior, give confidence in our results. In the phase velocity map at 60 s period (Figure 2d), broadly sensitive around 80 km depth, we see evidence of higher phase velocities in the region corresponding to the Pacific and Yakutat slabs subducting beneath interior Alaska (Eberhart-Phillips et al., 2006; Jiang et al., 2018; Martin-Short et al., 2018; Wang & Tape, 2014; Ward & Lin, 2018), as well as in the northern region corresponding to cold, thick lithosphere (Jiang et al., 2018; O'Driscoll & Miller, 2015).

Figure 3, similar to Figure 2, contains results derived from ambient noise cross correlations (Figures 3a and 3b) and from earthquakes (Figures 3c and 3d) but for H/V ratios and displaying both station measurements and underlying smoothed maps to enable interpretation of observations. In Figure 3a, corresponding to 10 s period and sensitive to highly shallow structure (≤1 km), we see high H/V ratios corresponding to the Yukon Flats, Cook Inlet Basin, Bethel Basin, Bristol Bay Basin, Copper River Basin, and in the northern part of the Cook Inlet. We see low H/V ratios, corresponding to crystalline rock, in the Brooks Range, Chugach Range, and Seward Peninsula. At 24 s period in Figure 3b, mostly sensitive to the upper crustal structure (<5 km), deeper parts of aforementioned basins and crystalline rock structures are visible as high and low H/V ratios, respectively. The consistency at 24 s period between ambient noise (Figure 3b) and earthquake Rayleigh waves (Figure 3c) provides confidence in our results. Figure 3d shows H/V ratios at 60 s which reflects upper to midcrustal structure of deep basins and crystalline features.

3.2. Shear Velocity Models and Sedimentary Thickness Results

Figure 4, the 1-D shear velocity result of the joint MCMC inversion, corresponds to Station I23K southwest of Minto, Alaska, on the outskirts of the Nenana Basin (yellow star, Figure 1). We observe a narrow posterior
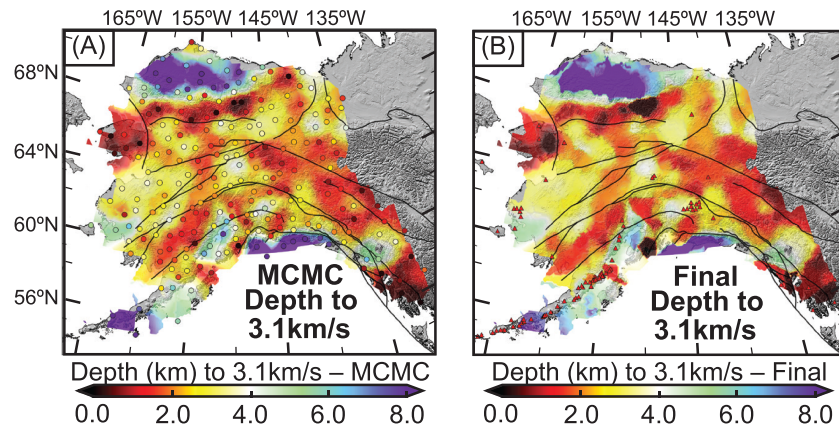
Figure 7. Final shear velocity model at (a) 1 km, (b) 25 km, (c) 45 km, and (d) 100 km depths with Holocene and Eocene volcanoes (red triangles) and major faults (black lines) overlaid for reference. Earthquakes (black dots) and the Yakutat Terrane (salmon outline, see Eberhart-Phillips, 2006) are also included in (d).

distribution (shown in cyan) of velocity models (Figures 4a and 4e–4h) that fit the data (Figures 4b–4d). Previous analysis of the Nenana Basin from well logs, gravity, and active-source seismic has mapped depth to basement below this station as ~2 km depth, corresponding to Vp between 4.5 and 5.3 km/s, or Vs 2.67–3.15 km/s (Brocher et al., 2005; Dixit et al., 2017; Tape et al., 2015), which matches our result at this station. In order to analyze approximate sediment thickness from the surface across the entirety of Alaska, while accounting for potentially faster basin material at depth, we show maps to Vs 3.1 km/s across the region for both MCMC and final Vs results in Figure 8. We note that although this is a higher estimate, it is below the lower end Vs associated with felsic material, for example, 3.2 km/s (Brocher, 2005).
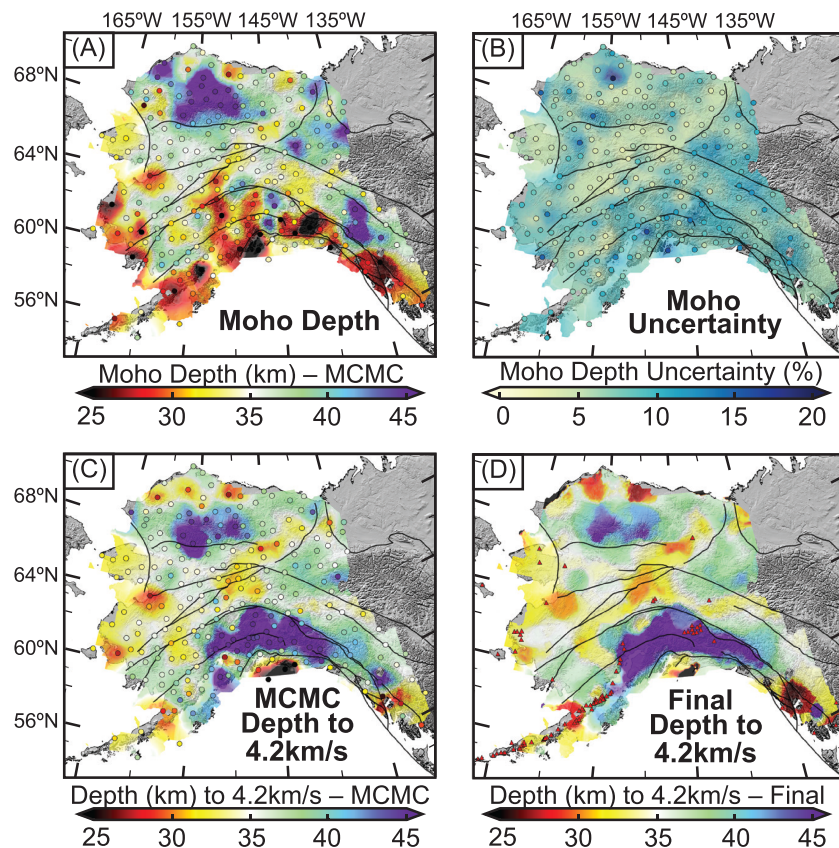
Figure 5, corresponding to results from the MCMC inversion, and Figure 7, our final shear velocity result, provide new regional insight into shallow through upper mantle features. After the joint inversion, which includes shallowly sensitive H/V ratios, the sedimentary basins are immediately apparent in Figures 5a and 7a, including the Colville, Cook Inlet, Copper River, Yukon Flats, Bethel, and Bristol Bay Basins (Krischner, 1994; Moore & Box, 2016; Plafker & Berg, 1994). Mountainous regions and those with similar geologic features (Plafker & Berg, 1994; Till, 2016) are also apparent as high-velocity regions, including the Brooks Range, Seward Peninsula, and Chugach mountains. The Selawik trough and Nenana Basin are clear but slightly less prominent than the other basins, the former because it is a shallow feature and the latter because we did not include stations directly within that basin. As the phase velocity measurements above 8 s period are not sensitive to near-surface structure, there are no apparent changes to the shallow results after the phase velocity-only inversion at this depth (Figure 7a). At 1 km depth, our results are strongly constrained as shown by the standard deviations at this depth in Figure 6a. However, the standard deviations are overall the widest at this depth compared to deeper results (Figures 6b–6d). This is most likely due to basin reverberations impacting receiver functions, complex near-surface layering, and potential issues from enforcing Vp and density derived from Vs.
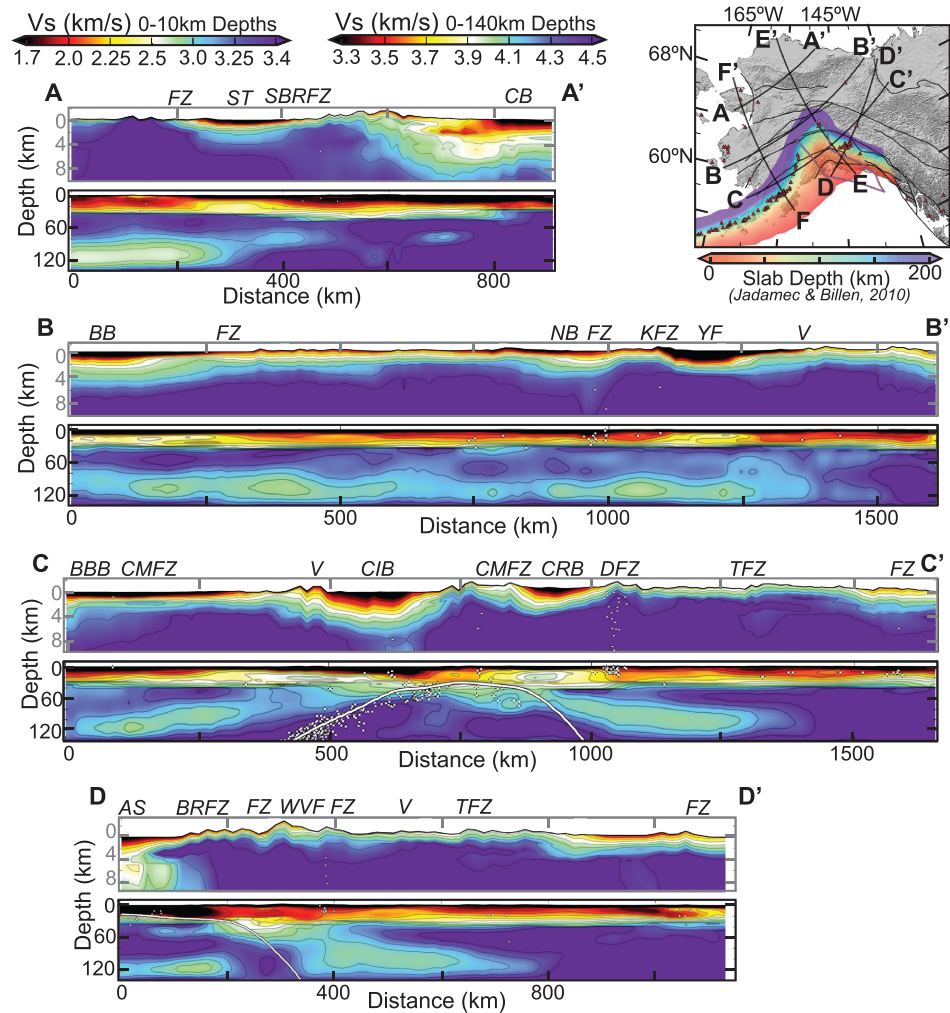
Figure 8. Depth to 3.1 km/s (approximate sedimentary basin thickness) from (a) MCMC joint inversion *Vs* results and (b) final *Vs* results.

From the map of depth to 3.1 km/s, estimating sediment thickness from both MCMC results (Figure 8a) and the final inversion (Figure 8b), basins are immediately apparent, and both results are similar due to the relatively poor sensitivity of phase velocity measurements above 8 s period to near-surface structure. Specifically, we see thick sediments within the Alaskan shelf, Colville Basin, and Cook Inlet Basin. The offshore component of Bethel Basin is relatively thick (~4–5 km), but shallows onshore. We also see that the Selawik Trough is very shallow (~3 km), while the Copper River Basin is deeper (~4 km). The Nenana Basin appears shallower than previously found, but this is most likely attributed to the narrow width of the basin. Both

Figure 9. (a) Moho depth following the MCMC inversion, (b) uncertainty in Moho depth parameter, (c) depth to 4.2 km/s from the MCMC inversion, and (d) depth to 4.2 km/s in the final result.
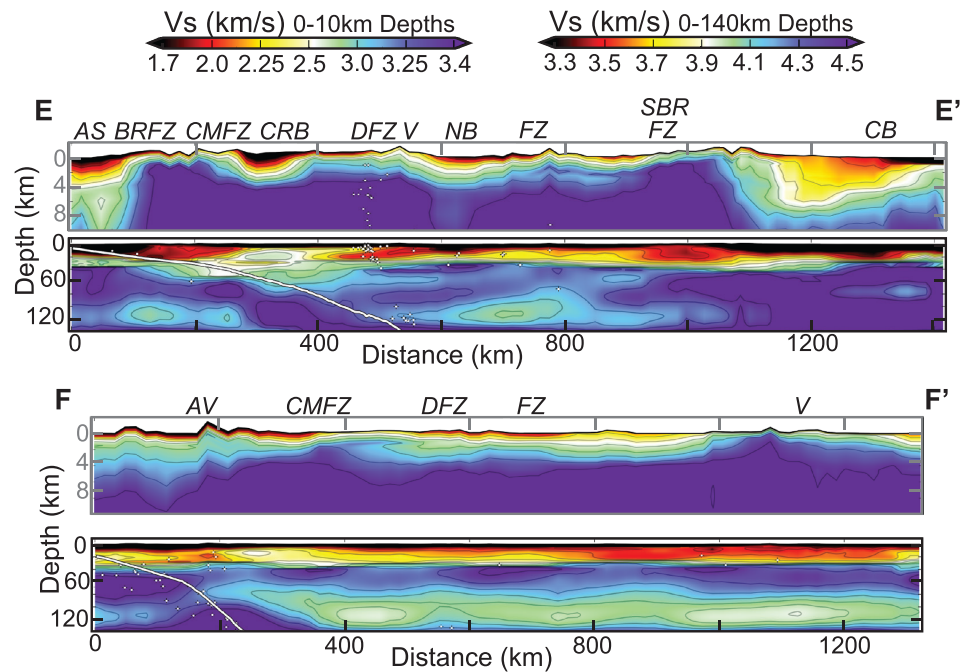
Figure 10. Cross sections A-A′ through D-D′ across Alaska (see upper right map). Fault zones are labeled as FZ (Denali, Castle Mountain, southern Brooks Range, Borders range, Tintina, and Kultag), volcanoes as V (Aleutian Volcanics and Wrangell volcanic field), and basins (Bethel, Bristol Bay, Colville, Copper River, cook inlet, Nenana, Yukon flats basins, and the Alaskan shelf). Earthquakes from Figure 1 are shown as white dot with an underlying black cross. Alaska_3D 1.0 slab model from Jadamec and Billen (2010) also included on applicable cross sections as a solid white line with a black outline.

Nenana and Yukon Flats Basins also suffer from station placement outside of the deeper parts of both basins, yielding shallower sediment thickness estimates. We note that previous tomography studies of Alaska that have aimed to resolve sediment thickness (Feng & Ritzwoller, 2019) and near-surface (<5 km) shear velocities (Feng & Ritzwoller, 2019; Ward & Lin, 2018) have not included H/V ratios. These studies report high uncertainties and poor sensitivity within their shallow results, and model comparison highlights the impact and importance of including H/V ratios to constrain the near surface as presented here.

At 25 km depth (Figures 5b and 7b), low velocities are observed in the Brooks Range, likely attributed to fold-and-thrust crustal thickening, below the Chugach mountain range, potentially related to underplated sediments, and near the WVF. Faster features are observed below the Cook Inlet Basin, potentially related to shallow mantle wedge structure or thin crust (Figure 10, Cross Section C-C′); Alaskan Shelf, related to the underlying Pacific plate; and in the interior of Alaska due to faster, harder crystalline rock of the Yukon Composite Terrane previously denoted in deep crustal studies (Brocher, 2004; Fuis et al., 2008). Our MCMC *Vs* results are strongly constrained for each station at 25 km depth (see Figure 6b); however, we see direct benefits from applying the follow-up phase velocity-only inversion at this depth (Figure 7b). Specifically, slower shear velocity is more strongly focused near the WVF, which was surrounded by

Figure 11. Cross sections E–E′ and F-F′ (see map in upper right corner of Figure 10), formatted similarly to Figure 10 cross sections.

stations but had no stations within the main volcanic field itself, and in the Brooks Range. Changes in velocity between the MCMC and phase velocity-only inversion are directly related to station distribution and demonstrate the benefit of a follow-up phase velocity inversion allowing interstation resolution.

At 45 km depth (Figures 5c and 7c), we see lower shear velocities below the Brooks Range, related to crustal thickening, and south of the Denali fault, related to the mantle wedge above the subducting Yakutat and Pacific slabs. In Figure 7c, the mantle wedge stretches into the Aleutian arc, similar to previous studies (Martin-Short et al., 2018; Ward & Lin, 2018). However, this is near the edge of our model where there are fewer measurements and poorer azimuthal coverage that may impact ambient noise-derived data. At 100 km depth, there is evidence of the subducting Pacific slab, as well as western and eastern asthenosphere in both Figures 5d and 7d. Both 45 km (Figures 5c and 7c) and 100 km (Figures 5d and 7d) depths show strong constraint from the standard deviation of the posterior model (Figures 6c and 6d) from the MCMC results, although minor adjustments mainly attributed to smoothing inherent to the phase velocity-only inversion can be seen. Within the cross sections (Figures 10 and 11) we have included the Alaska_3D 1.0 slab model from Jadamec and Billen (2010), which includes a bend near the Denali fault, similar to our results.

3.3. Moho Depth and Crustal Thickness Results

We show Moho depth and uncertainty in Figures 9a and 9b, respectively, but note that the Moho depth here merely shows the depth from the surface to the bottom of the layer with four B-splines that roughly represents the crust. Although this parameter is relatively certain following the MCMC inversion (Figure 9b), there is wide scatter in the map of Moho depth (Figure 9a). This may be in part an effect of the parametrization that does not allow intracrustal interfaces between the bottom of the linear sediment layer and the Moho. Previous work using xenoliths as ground truth shows that if a distinct high-velocity lower crustal layer exists, receiver functions and surface waves may pick up the top of such a layer as the Moho, rather than the petrological crust–mantle boundary (Schulte-Pelkum et al., 2017). The same study showed that while it is technically easy to build in an additional lower crustal velocity contrast, achieving decreased misfit across a large area with such additional parametrization is difficult. We interpret the Moho from our results with this caveat in mind. We see a relatively deep Moho near the Brooks Range and to the north. We also see a shallower thin stretch of shallower Moho near central Alaska along the Tintina-Kultag fault, although previous studies have described a slightly shallower Moho within the Yukon Composite Terrane

(Fuis et al., 2008; Miller, 2018). We also see a shallower Moho southeast of the WVF and along the western portion of Alaska from the Seward Peninsula and reaching southwest although with wide variation, similar to previous results (Miller et al., 2018). We also observe a sharp transition across the Denali fault from deep to shallow from north to south, opposing previous studies (Allam et al., 2017; Miller, 2018), although significant scatter throughout our results in this area makes it difficult to identify a definitive trend.

In order to better constrain the depth to the mantle, we also include maps of depth to 4.2 km/s after the MCMC inversion (Figure 9c) and the final phase velocity-only inversion (Figure 9d). Although depth to 4.2 km/s may not represent the Moho at every location, this is another viable approach to evaluate the approximate crustal thickness while also enabling comparison of the MCMC and final *Vs* model results. We observe greater depths (>45 km) in the northern part of Alaska, constrained near the Brooks Range, and south of the Denali fault in both MCMC and Final *Vs* models (Figures 9c and 9d, respectively). We do note that although depths are greater south of the Denali fault via the metric of depth to 4.2 km/s, we are likely capturing a depth to below the hydrated mantle wedge (see section 4.2) and therefore overestimating crustal thickness in this area. In both models we also consistently observe shallower depths (30–35 km depths) beneath the Yukon Composite Terrane, along the western side of the Colville Basin, northeast of the WVF, the region from the Seward Peninsula toward the Bethel Basin in eastern Alaska, and a northwest-southeast trend reaching from the Castle Mountain fault, near the Aleutian arc, to the Kaltag fault zone. A small area of very thin crust is observed on the eastern edge of the Colville Basin, north of the Brooks Range. Major differences include the Cook Inlet and Bethel Basin, which are both strongly impacted by basin effects and shallow multiples within the receiver functions that are mitigated in the follow-up inversion.

4. Discussion

4.1. Basin Structure

With the improved shallow sensitivity from the inclusion of H/V ratios, we provide new constraints on shallow crustal structure on a regional scale (Lin et al., 2012, 2014; Tanimoto & Rivera, 2008). Resolving upper crustal structure is critical as this allows improvements in ground motion predictions (Graves et al., 2011; Vidale & Helmberger, 1988), insight into lithospheric discontinuities (Langston, 2011), and validation of geological interpretations based on direct surface observations (e.g., Graymer et al., 2005). In particular, the geometry of near-surface sedimentary basins is well known to exert strong controls on the coseismic wavefield of large earthquakes (e.g., Bowden & Tsai, 2017; Olsen, 2000; Wang et al., 2016), effectively amplifying coseismic shaking by trapping energy in low-velocity sedimentary rocks. Our results include a complete tomographic map of every major basin in Alaska (Figures 5a, 7a, 8a, and 8b) including the Colville Basin, Selawik Trough, Yukon Flats Basin, Nenana Basin, Copper River Basin, Cook Inlet Basin, Bethel Basin, Bristol Bay Basin, and the Alaskan shelf.

The Colville Basin is a 1–12 km deep, ~600 km-by-150 km wide foreland basin located in Arctic Alaska, north of the Brooks Range, most notable for interest in hydrocarbon resources (Saltus & Bird, 2003). The basin deepens to the south due to the interaction of the underlying south dipping Barrow arch (Bird, 2001; Grantz et al., 1994; Saltus & Bird, 2003) and the detritus mainly derived in the late Jurassic and Early Cretaceous in response to Brooks Range uplift, crustal shortening, and fold-and-thrust belts (Grantz et al., 1994; Till, 2016). Our modeled structure (Figure 8; Figure 10, A-A′; and Figure 11, E–E′) within the Colville Basin and Brooks range is consistent with active source seismic surveys, well logs, and gravity and aeromagnetic analyses (Cole et al., 1997; Grantz et al., 1994; Nunn et al., 1987; Saltus et al., 2006; Saltus & Bird, 2003). We also observe similar shear velocities throughout the Seward Peninsula and Brooks Range, consistent with geology and tectonic ties between the two areas (Cole et al., 1997; Moore & Box, 2016; Till, 2016; Wilson et al., 2015).

The Nenana Basin is primarily a transtensional basin related to the crustal extension and strike-slip faulting accommodated by the Denali fault to the south and Tintina-Kaltag system to the north (Page et al., 1995; Tape et al., 2015; Van Kooten et al., 2012). Sediments within the basin include lacustrine and fluvial deposits related to crustal extension during the late Paleocene (Dixit et al., 2017; Van Kooten et al., 2012), Eocene regional uplift (Dixit et al., 2017), and Miocene rifting and subsidence followed by Pliocene and Quaternary transtensional pull-apart processes. The Nenana Basin (Figure 10, B-B′ and Figure 11, E–E′) is

largely shallow but reaches a maximum depth of ~10 km in a SW–NE trending linear trend (Van Kooten et al., 2012) consistent with its transtensional formation history. Although we do not fully capture this narrow, linear basin mainly due to limitations from station distribution, we do observe a subdued similar feature in our B-B′ and E-E′ cross sections (from Figures 10 and 11, respectively).

The Cook Inlet Basin is bounded to the south by the Border Ranges fault system, which separates the basin from the Chugach terrane and associated Kenai and Chugach mountains (Mankhemthong et al., 2013; Shellenbaum et al., 2010). This forearc basin with Mesozoic to Quaternary deposits formed within the Wrangellia Composite Terrane during the Paleocene-Eocene uplift of the Alaskan Range (Benowitz et al., 2012; Finzel, 2010; Plafker & Berg, 1994; Ridgway et al., 2011) followed by nonuniform glacial deposits (Plafker & Berg, 1994; Shellenbaum et al., 2010). Previous borehole and seismic surveys determined total sediment thickness varies from ~1.5 km along the north bounding Castle Mountain fault and south bounding Border Ranges fault, to ~8.5 km depth in the center of the Cook Inlet (Plafker et al., 1989; Shellenbaum et al., 2010), all of which we observe in our cross section (Figure 10, C-C′) and map view (Figures 8a and 8b) results.

The Copper River Basin lies northwest of the WVF and is bounded to the north by the Denali fault. The basin initiated in the Upper Cretaceous due to curvature of the Denali fault, and consists of Oligocene fluvial and Cretaceous marine sand to siltstones overlain by Quaternary glacial and alluvial sediments (Andreasen et al., 1958; Fuis et al., 1989; Schultz & Aydin, 1990). This basin is shallowest adjacent to the Denali fault zone and deepens southward to a maximum of 4 km (Figure 10, C-C′ and Figures 8a and 8b), consistent with previous active-source studies (Fuis et al., 1989).

The backarc, mostly offshore, Bristol Bay Basin lies on the north side of the Aleutian Islands on the Bering Sea Shelf. The deepest part of the basin (more than 6 km) contains Cenozoic deposits onshore and offshore of the Aleutian arc, southwest of Kodiak Island on the northwest side of the arc, and shallows northward onshore and offshore of mainland Alaska (Finzel et al., 2009; Kirschner, 1994). We best resolve the onshore portion and clearly observe low velocities in the upper 2–3 km (Figure 10, C-C′ and Figures 8a and 8b) shallowing further onshore within mainland Alaska. Additionally, we potentially image deeper sediments on the northwest side of the arc (Figures 8a and 8b).

We also resolve several additional small-scale basins. Bethel Basin lies northeast of the Bering Sea and contains a relatively thin (<0.5 km) Tertiary deposit overlying ~4 km of Cretaceous sedimentary rock (Kirschner, 1994); we clearly observe the Bethel Basin in Figure 10, B-B′ cross section and Figures 8a and 8b. The Selawik Trough, east of the Seward Peninsula between the South Brooks Range fault system and the Kugruk fault zone, is a relatively small feature containing <3 km of Cenozoic fill (Decker, 1988; Kirschner, 1994) observed in Figure 10, A-A′ and Figures 8a and 8b. The Yukon Flats Basin is associated with nonmarine sediments of Cretaceous to early Tertiary age produced by extension and right-lateral movement along the Tintina fault system (Kirschner, 1994; Schultz & Aydin, 1990; Till et al., 2006). Although gravity and aeromagnetic interpretations suggest a basin depth to be around 4 km for the majority of the basin (Phillips & Saltus, 2005; Till et al., 2006; Van Kooten et al., 2012), we observe a slightly shallower feature around 3 km depth (Figure 8 and Cross Section B-B′ from Figure 10). This is due to limited station coverage (Figure 1) and strong reverberations within the receiver functions that make fitting the data during the inversion process difficult (see Figure 6a).

4.2. Lithospheric Structure

In order to examine variations in crustal thickness, we show both maps of the Moho determined from the MCMC joint inversion (Figure 9a) as well as spatial maps of depth to 4.2 km/s shear wave velocity after the joint inversion (Figure 9c) and the final inversion (Figure 9d), as >4.2 km/s is more typical of upper mantle compositions (Ward & Lin, 2018). We observe a similar pattern to previous studies (Allam et al., 2017; Miller et al., 2018; O'Driscoll & Miller, 2015; Ward & Lin, 2018) with a shallow Moho beneath the Yukon Composite Terrane (~30 km) and deeper Moho beneath the Brooks Range before shallowing north of the Brooks Range. This overall pattern is also clear in Figure 11 Cross Section E–E′. The Moho structure beneath the Brooks Range has been particularly well studied with deep seismic reflection and refraction surveys (Cole et al., 1997; Fuis et al., 1995), gravity analyses (Nunn et al., 1987; Saltus et al., 2006), and regional tomography results (Jiang et al., 2018; Martin-Short et al., 2018; Ward & Lin, 2018), all in agreement with our

present results. We additionally observe a wedge of faster crustal material in the northern Brooks Range (Figures 7b and 11, E–E′ cross section), associated either with Cenozoic thin-skinned fold-and-thrust deformation (Ward & Lin, 2018) or a voluminous mafic root related to the north slope magnetic high/boundary (Saltus & Hudson, 2007). Maps of depth to 4.2 km/s (Figures 9c and 9d) suggest thicker crust (>45 km) south of the Denali Fault within the Wrangellia Composite Terrane. However, this could instead potentially be attributed to a hydrated mantle wedge structure (see section 4.3 for discussion) and a shallower, more complex (<45 km) Moho, as suggested in Figure 9a.

Variations in crustal thickness can more generally be attributed to changes among the individual terranes, specifically the Arctic Alaska, Yukon Composite, and Wrangellia Composite Terranes. These changes are similar to long-wavelength (>75 km) Bouguer gravity anomalies with lower gravity seen in areas of thicker crust (e.g., Brooks Range) and higher gravity in areas with thinner crust (e.g., Yukon Composite Terrane) (Bonvalot et al., 2012; Ward & Lin, 2018). Additionally, we observe a small area (~100 km wide) north of the Brooks Range on the eastern edge of the Colville Basin with a very shallow depth to Moho (Figures 9a and 9b) and to 4.2 km/s (Figures 9c and 9d). This area contains ~5 km sediment thickness (Saltus & Bird, 2003) and is underlain by a low-Vs, low-density basement (Saltus et al., 2006) as shown in A-A′ cross section (from Figure 10). This anomalous area has previously been observed but is still of unknown provenance (Saltus et al., 2006; Saltus & Bird, 2003).

At 100 km depth (Figures 5d and 7d), we observe the highest shear velocities of the entire model north of the Brooks Range and the region northeast of the Yukon Flats Basin, corresponding to a cold, thick, cratonic mantle root that impacts deformation to the south, as discussed in previous studies (Jiang et al., 2018; O'Drisoll & Miller, 2015; Saltus & Hudson, 2007). At this depth, we also observe fast shear velocities in the subducting Pacific plate, similar to previous studies (Eberhart-Phillips et al., 2006;Jiang et al., 2018 ; Martin-Short et al., 2018). Due to relatively warm and shallow lithosphere-asthenosphere boundary, we observe low velocities in both western and eastern Alaska, as interpreted in previous regional tomography studies (Jiang et al., 2018; Martin-Short et al., 2018). Though we lack resolution to observe individual volcanic plumes, we note that the lower velocities of the asthenosphere appear to shallow in western Alaska and could provide a source for the Bering Sea, Seward Peninsula, and Eastern Aleutian volcanism as potentially suggested by sparse geochemical (Akinin et al., 1997; Johnson et al., 1996; Nye & Reid, 1986; Tappen et al., 2009) and stress (Tibaldi & Bonali, 2017) data. Our results support the hypothesis of a broad, hot backarc in the western Alaskan subduction zone (Curie & Hyndman, 2006).

4.3. Mantle Wedge

At 45 km depth (Figures 5c and 7c), we observe lower velocities (~4.1 km/s) beneath the Wrangellia Composite Terrane, south of the Denali fault, which indicates the presence of a hydrated mantle wedge, although we are not able to determine from our model the extent of hydrous fluids versus melt (Jiang et al., 2018; Martin-Short et al., 2018; Ward & Lin, 2018). This also suggests that the Moho transition from continental crust to mantle is shallower than the depth shown in Figures 9c and 9d as these maps represent depth to 4.2 km/s. In this region, depth to 4.2 km/s corresponds to depths within the mantle wedge, or the transition from mantle wedge to underlying subducting oceanic plate. Instead, the Moho is likely shallower (Figures 10, C-C′; 10, D-D′; and 11, E–E′), as presented across most of the Wrangellia Composite Terrane in Figure 9a of the Moho depth from the MCMC joint inversion. The mantle wedge structure, shown as a relatively slow anomaly with Vs of ~4.1 km/s, covers both the volcanically active Aleutian arc and nonactive Denali Volcanic Gap (Figures 10, C-C′; 10, D-D′; and 11, E–E′). This has previously been interpreted as a region of high attenuation (Stachnik et al., 2004) related to serpentinization due to the onset of fluid release from eclogitization of downgoing oceanic crust (Martin-Short et al., 2018), which depresses seismic velocities in the overlying mantle wedge. As previously noted (Martin-Short et al., 2018), this wedge has been associated with a relatively low (≤30%) level of serpentinization compared to Cascadia from Vp/Vs models (Rossi et al., 2006) and noninverted Moho (Bostock et al., 2002). However, thermal modeling results suggest that dehydration within most subduction zones, including that in southern Alaska, is too slow to support significant serpentinization to lower seismic velocities. Instead, alternative subduction zone processes, such as inclusion of crustal velocity material in the wedge may contribute to the reduction of seismic velocities (Abers et al., 2017; Ward & Lin, 2018).

We observe a north dipping lithosphere-asthenosphere boundary in the North American plate northeast of the Aleutian arc, as shown in Cross Section F-F′ (Figure 11) that complements findings of Martin-Short et al. (2018). Specifically, the lithosphere-asthenosphere boundary dips to the north until the Castle Mountain Fault Zone, where it remains relatively flat throughout the northwestern side of the cross section. In this region, fluids released from the slab at 100 km depth can interact with the asthenosphere to contribute to melt production and volcanism. In contrast, the asthenosphere beneath the Denali volcanic gap (Figure 11, E–E′) is deeper and relatively flat, with shear velocities higher than western Alaska (see Figure 11, F-F′); we infer that the slab is not dehydrating in this area, and thus, melt is not being produced, creating the volcanic gap. Additionally, as discussed by Martin-Short et al. (2018), the subducting Yakutat Terrane is younger and warmer than the Pacific plate and is thus associated with shallow dehydration (Chuang et al., 2017) and a thicker overall lithosphere containing the continental and oceanic (Pacific and overriding Yakutat) terranes (Eberhart-Phillips et al., 2006; Martin-Short et al., 2018). This indicates that the terrane is relatively anhydrous compared to the Pacific plate which would further contribute to a lack of volcanism and seismicity.

4.4. WVF and Yakutat Slab

We observe a low-velocity zone beneath the WVF around 25 km depth (Figure 7b and Cross Section D-D′ in Figure 10), potentially corresponding to a low-melt percentage magma reservoir. Previous studies in this region have either lacked shallow resolution or have been focused on other structure, but our results could provide insight and allow new interpretation of the complicated geochemical data associated with the WVF. (e.g., Preece & Hart, 2004; Skulki et al., 1994; Trop et al., 2012). We observe that the high-Vs edge of the Yakutat slab (Figure 10, C-C′ and D-D′) is adjacent to the western edge of the WVF; the Yakutat slab could contribute to Wrangell volcanism in two ways. The first is through upwelling and quasi-toroidal flow of asthenosphere against the western edge of the slab, suggested by geodynamic modeling (Jadamec & Billen, 2010, 2012) and the northwest advance of the WVF over the past 23 Ma as the Yakutat also progressed northwestward (Martin-Short et al., 2018). Second, the presence of adakites in the western WVF suggests that melting of the Yakutat slab itself contributed to volcanism (Martin-Short et al., 2018; Preece & Hart, 2004).

We do not see evidence of a fast-Vs Wrangell slab beneath the WVF as suggested by Jiang et al. (2018), but we do observe fast Vs at ~70 km northeast of the WVF (see Cross Section D-D′ in Figure 11). Our results in this region support and add to imaging from Martin-Short et al. (2018). As shown at 100 km depth (Figures 5d and 7d), we observe lower velocities in the region surrounding and east of the volcanic field, supporting evidence of a lithosphere-asthenosphere boundary and asthenosphere contribution to Wrangell volcanism. The asthenosphere is also clearly seen in Cross Section D-D′ below the Yakutat Terrane and northeast of the WVF.

5. Conclusions

By combining Rayleigh wave H/V ratios, phase velocities, and receiver functions, we obtain a 3-D shear wave velocity model with resolution from the shallow crust (≥1 km) through the upper mantle. We discuss the similarities of our findings in the Alaskan basins to previous geological and geophysical studies, provide new constraints on basin and tectonic structure, and explore midcrustal findings of potential evidence for the presence of magma reservoirs beneath the WVF. We analyze regional variations of crustal thickness in relation to different terranes and image the mantle wedge and discuss its relation to volcanism in southern Alaska. Finally, we discuss the potential impact of asthenosphere flow and serpentinization on the Aleutian volcanic arc compared to the Denali volcanic gap, as well as in the WVF with the impact of the Yakutat Terrane. Our detailed model can be used as a basis for comparison and integration with subsequent geological, geochemical, and geophysical studies across all of Alaska.

References

Abers, G. A., van Keken, P. E., & Hacker, B. R. (2017). The cold and relatively dry nature of mantle forearcs in subduction zones. *Nature Geoscience*, *10*(5), 333–337. https://0120100299/10.1038/ngeo2922

Allam, A. A., Schulte-Pelkum, V., Ben-Zion, Y., Tape, C., Ruppert, N., & Ross, Z. E. (2017). Ten kilometer vertical Moho offset and shallow velocity contrast along the Denali fault zone from double-difference tomography, receiver functions, and fault zone head waves. *Tectonophysics*, *721*, 56–69. https://0120100299/10.1016/j.tecto.2017.09.003

Anderson, E. D., Hitzman, M. W., Monecke, T., Bedrosian, P. A., Shah, A. K., & Kelley, K. D. (2013). Geological analysis of aeromagnetic data from southwestern Alaska: Implications for exploration in the area of the Pebble porphyry Cu-Au-Mo deposit. *Economic Geology*, *108*(3), 421–436. https://0120100299/10.2113/econgeo.108.3.421

Andreasen, G. E., Dempsey, W. J., Henderson, J. R., & Gilbert, F. P. (1958). *Aeromagnetic map of the Copper River basin. Alaska: U.S. Geological Survey Geophysical Investigations. USGS Numbered Series Report (Map No.156)*. https://0120100299/10.3133/gp156, https://pubs.er.usgs.gov/publication/gp156

Benowitz, J. A., Haeussler, P. J., Layer, P. W., O'Sullivan, P. B., Wallace, W. K., & Gillis, R. J. (2012). Cenozoic tectono-thermal history of the Tordrillo Mountains, Alaska: Paleocene-Eocene ridge subduction, decreasing relief, and late Neogene faulting. *Geochemistry, Geophysics, Geosystems*, 13 Q04009. https://0120100299/10.1029/2011GC003951

Bensen, G. D., Ritzwoller, M. H., Barmin, M. P., Levshin, A. L., Lin, F., Moschetti, M. P., et al. (2007). Processing seismic ambient noise data to obtain reliable broad-band surface wave dispersion measurements. *Geophysical Journal International*, *169*(3), 1239–1260. https://0120050077/10.1111/j.1365-246X.2007.03374.x

Berg, E. M., Lin, F. C., Allam, A., Qiu, H., Shen, W., & Ben-Zion, Y. (2018). Tomography of Southern California via Bayesian joint inversion of Rayleigh wave ellipticity and phase velocity from ambient noise cross-correlations. *Journal of Geophysical Research: Solid Earth*, *123*(11), 9933–9949. https://0120050077/10.1029/2018JB016269

Bird, K. J. (2001). *Framework geology, petroleum systems, and play concepts of the National Petroleum Reserve, Alaska*. Society for Sedimentary Geology (Core Workshop 21) (pp. 5–17).

Bonvalot, S., Balmino, S., Briais, A., Kuhn, M., Peyrefitte, A., & Vales, N. (2012). *World gravity map, Bureau Gravimetrique International (BGI)*. Paris: CGMW-BGI-CNES-IRD.

Bowden, D. C., & Tsai, V. C. (2017). Earthquake ground motion amplification for surface waves. *Geophysical Research Letters*, *44*(1), 121–127. https://0120050077/10.1002/2016GL071885

Brocher, T. (2005). Empirical relations between elastic wavespeeds and density in the Earth's crust. *Bulletin of the Seismological Society of America*, *95*(6), 2081–2092. https://0120050077/0120050077/0120050077

Bruhn, R. L., & Haeussler, P. J. (2006). Deformation driven by subduction and microplate collision: Geodynamics of Cook Inlet basin, Alaska. *Geological Society of America Bulletin*, *118*(3–4), 289–303. https://0120050077/10.1130/B25672.1

Christeson, G. L., Gulick, S. P. S., van Avendonk, H. J. A., Worthington, L. L., Reece, R. S., & Pavlis, T. L. (2010). The Yakutat terrane: Dramatic change in crustal thickness across the transition fault, Alaska. *Geology*, *38*(10), 895–898. https://0120050077/10.1130/G31170.1

Chuang, L., Bostock, M., Wech, A., & Plourde, A. (2017). Plateau subduction, intraslab seismicity, and the Denali (Alaska) volcanic gap. *Geology*, *45*(7), 647–650. https://0120050077/10.1130/G38867.1

Cole, F., Bird, K. J., Toro, J., Roure, F., O'Sullivan, P. B., Pawlewicz, M., & Howelll, D. G. (1997). An integrated model for the tectonic development of the frontal Brooks Range and Colville Basin 250 km west of the Trans-Alaska Crustal Transect. *Journal of Geophysical Research*, *102*(B9), 20,685–20,708. https://0120050077/10.1029/96JB03670

Coleman, J. L., & Cahan, S. M. (2012). Preliminary catalog of the sedimentary basins of the United States. US Department of the Interior, US Geological Survey Open-File Report 2012–1111

Colpron, M., Nelson, J. L., & Murphy, D. C. (2007). Northern Cordilleran terranes and their interactions through time. *GSA Today*, *17*(4/5), 4. https://0120050077/10.1130/GSAT1704-5A.1

Decker, J., Robinson, M. S., Clough, J. G., & Lyle, W. M. (1988). *Geology and petroleum potential of Hope and Selawik Basins. Alaska Div. Geol. Geophys. Surv. Public Data File Rep.*, *88–1*, 29.

Dixit, N., Hanks, C., Rizzo, A., McCarthy, P., & Coakley, B. (2017). Cenozoic tectonic and thermal history of the Nenana basin, central interior Alaska: New constraints from seismic reflection data, fracture history, and apatite fission-track analyses. *Canadian Journal of Earth Sciences*, *54*(7), 766–784. https://0120050077/10.1139/cjes-2016-0197

Eberhart-Phillips, D., Christensen, D. H., Brocher, T. M., Hansen, R., Ruppert, N. A., Haeussler, P. J., & Abers, G. A. (2006). Imaging the transition from Aleutian subduction to Yakutat collision in central Alaska, with local earthquakes and active source data. *Journal of Geophysical Research*, *111*(B11). https://0120050077/10.1029/2005JB004240

Feng, L., & Ritzwoller, M. H. (2019). A 3-D shear velocity model of the crust and uppermost mantle beneath Alaska including apparent radial anisotropy. *Journal of Geophysical Research: Solid Earth*. https://0120050077/10.1029/2019JB018122

Finzel, E. S., Ridgway, K. D., Reifenstuhl, R. R., Blodgett, R. B., White, J. M., & Decker, P. L. (2009). Stratigraphic framework and estuarine depositional environments of the Miocene Bear Lake Formation, Bristol Bay Basin, Alaska: Onshore equivalents to potential reservoir strata in a frontier gas-rich basin. *AAPG Bulletin*, *93*(3), 379–405. https://0120050077/10.1306/10010808030

Finzel, E. S., Trop, J. M., Ridgway, K. D., & Enkelmann, E. (2011). Upper plate proxies for flat-slab subduction processes in southern Alaska. *Earth and Planetary Science Letters*, *303*(3–4), 348–360. https://0120050077/10.1016/j.epsl.2011.01.014

Fuis, G. S., Ambos, E. L., Mooney, W. D., & Christensen, N. I. (1989). Summary of deep structure of accreted terranes in the Chugach Mountains and Copper River Basin, Southern Alaska from seismic refraction results. *Alaskan Geological and Geophysical Transect*, *104*, 23–26. https://0120050077/10.1029/FT104p0023

Fuis, G. S., Moore, T. E., Plafker, G., Brocher, T. M., Fisher, M. A., Mooney, W. D., et al. (2008). Trans-Alaska crustal transect and continental evolution involving subduction underplating and synchronous foreland thrusting. *Geology*, *36*(3), 267–270. https://0120050077/10.1130/G24257A.1

Grantz, A., May, S. D., & Hart, P. E. (1994). Geology of the Arctic continental margin of Alaska. In H. C. Berg (Ed.), *Plafker, George* (pp. 17–48). Geological Society of America: The geology of Alaska.

Graves, R., Jordan, T. H., Callaghan, S., Deelman, E., Field, E., Juve, G., et al. (2011). CyberShake: A physics-based seismic hazard model for Southern California. *Pure and Applied Geophysics*, *168*(3–4), 367–381. https://0120050077/10.1007/s00024-010-0161-6

Graymer, R. W., Ponce, D. A., Jachens, R. C., Simpson, R. W., Phelps, G. A., & Wentworth, C. M. (2005). Three-dimensional geologic map of the Hayward fault, Northern California: Correlation of rock units with variations in seismicity, creep rate, and fault dip. *Geology*, *33*(6), 521–524. https://0120050077/10.1130/G21435.1

Haeussler, P. J., Bruhn, R. L., & Pratt, T. L. (2000). Potential seismic hazards and tectonics of the upper Cook Inlet basin, Alaska, based on analysis of Pliocene and younger deformation. *Geological Society of America Bulletin*, *112*(9), 1414–1429. https://0120050077/10.1130/0016-7606(2000)112%3C1414:PSHATO%3E2.0.CO;2

Herrmann, R. B., & Ammon, C. J. (2004). *Surface waves, receiver functions and crustal structure, in Computer Programs in Seismology, Version3.30*. Saint Louis University. Retrieved from http://www.eas.slu.edu/People/RBHerrmann/CPS330.html

Jadamec, M., & Billen, M. I. (2012). The role of rheology and slab shape on rapid mantle flow: Three-dimensional numerical models of the Alaska slab edge. *Journal of Geophysical Research*, *117*, B02304. https://0120050077/10.1029/2011JB008563

Jadamec, M. A., & Billen, M. I. (2010). Reconciling surface plate motions with rapid three-dimensional mantle flow around a slab edge. *Nature*, *465*(7296), 338–341. https://0120050077/10.1038/nature09053

Jadamec, M. A., Billen, M. I., & Roeske, S. M. (2013). Three-dimensional numerical models of flat slab subduction and the Denali fault driving deformation in south-central Alaska. *Earth and Planetary Science Letters*, *376*, 29–42. https://0120050077/10.1016/j.epsl.2013.06.009

Jiang, C., Schmandt, B., Ward, K. M., Lin, F. C., & Worthington, L. L. (2018). Upper mantle seismic structure of Alaska from Rayleigh and S wave tomography. *Geophysical Research Letters*, *45*(19), 10–350. https://0120050077/10.1029/2018GL079406

Johnson, K. E., Harmon, R. S., Richardson, J. M., Moorbath, S., & Strong, D. F. (1996). Isotope and trace element geochemistry of Augustine Volcano, Alaska: Implications for magmatic evolution. *Journal of Petrology*, *37*(1), 95–115. https://0120050077/10.1093/petrology/37.1.95

Kirschner, C. E. (1994). *Interior basins of Alaska. The geology of North America series* (Vol. G-1, p. 469, 493). America: Geological Society.

Langston, C. A. (1977). Corvallis, Oregon, crustal and upper mantle receiver structure from teleseismic P and S waves. *Bulletin of the Seismological Society of America*, *67*(3), 713–724.

Langston, C. A. (1979). Structure under Mount Rainier, Washington, inferred from teleseismic body waves. *Journal of Geophysical Research*, *84*(B9), 4749–4762. https://0120050077/10.1029/JB084iB09p04749

Langston, C. A. (2011). Wave-field continuation and decomposition for passive seismic imaging under deep unconsolidated sediments. *Bulletin of the Seismological Society of America*, *101*(5), 2176–2190. https://0120050077/10.1785/0120100299

Ligorría, J. P., & Ammon, C. J. (1999). Iterative deconvolution and receiver-function estimation. *Bulletin of the Seismological Society of America*, *89*(5), 1395–1400.

Lin, F.-C., Moschetti, M. P., & Ritzwoller, M. H. (2008). Surface wave tomography of the western United States from ambient seismic noise: Rayleigh and Love wave phase velocity maps. *Geophysical Journal International*, *173*(1), 281–298. https://0120050077/10.1111/j.1365-246X.2008.03720.x

Lin, F. C., & Ritzwoller, M. H. (2011). Helmholtz surface wave tomography for isotropic and azimuthally anisotropic structure. *Geophysical Journal International*, *186*(3), 1104–1120. https://0120050077/10.1111/j.1365-246X.2011.05070.x

Lin, F.-C., Ritzwoller, M. H., & Snieder, R. (2009). Eikonal tomography: Surface wave tomography by phase front tracking across a regional broad-band seismic array. *Geophysical Journal International*, *177*(3), 1091–1110. https://0120050077/10.1111/j.1365-246X.2009.04105.x

Lin, F.-C., Schmandt, B., & Tsai, V. C. (2012). Joint inversion of Rayleigh wave phase velocity and ellipticity using USArray: Constraining velocity and density structure in the upper crust. *Geophysical Research Letters*, *39*, L12303. https://0120050077/10.1029/2012GL052196

Lin, F.-C., Tsai, V. C., & Schmandt, B. (2014). 3-D crustal structure of the western United States: Application of Rayleigh-wave ellipticity extracted from noise cross-correlations. *Geophysical Journal International*, *198*(2), 656–670. https://0120050077/10.1093/gji/ggu160

Mankhemthong, N., Doser, D. I., & Pavlis, T. L. (2013). Interpretation of gravity and magnetic data and development of two-dimensional cross-sectional models for the Border Ranges fault system, south-central Alaska. *Geosphere*, *9*(2), 242–259. https://0120050077/10.1130/GES00833.1

Martin-Short, R., Allen, R., Bastow, I. D., Porritt, R. W., & Miller, M. S. (2018). Seismic imaging of the Alaska Subduction Zone: Implications for slab geometry and volcanism. *Geochemistry, Geophysics, Geosystems*, *19*(11), 4541–4560. https://0120050077/10.1029/2018GC007962

Miller, M. S., & Moresi, L. (2018). Mapping the Alaskan Moho. *Seismological Research Letters*, *89*(6), 2430–2436. https://0120050077/10.1785/0220180222

Moore, T. E., & Box, S. E. (2016). Age, distribution and style of deformation in Alaska north of 60°N: Implications for assembly of Alaska. *Tectonophysics*, *691*, 133–170. https://0120050077/10.1016/j.tecto.2016.06.025

Nunn, J. A., Czerniak, M., & Pilger, R. H. Jr. (1987). Constraints on the structure of Brooks Range and Colville Basin, Northern Alaska, from flexure and gravity analysis. *Tectonics*, *6*(5), 603–617. https://0120050077/10.1029/TC006i005p00603

Nye, C. J., & Reid, M. R. (1986). Geochemistry of primary and least fractionated lavas from Okmok volcano, central Aleutians: Implications for arc magmagenesis. *Journal of Geophysical Research*, *91*(B10), 10,271–10,287. https://0120050077/10.1029/JB091iB10p10271

O'Driscoll, L. J., & Miller, M. S. (2015). Lithospheric discontinuity structure in Alaska, thickness variations determined by Sp receiver functions. *Tectonics*, *34*, 694–714. https://0120050077/10.1002/2014TC003669

Olsen, K. B. (2000). Site amplification in the Los Angeles basin from three-dimensional modeling of ground motion. *Bulletin of the Seismological Society of America*, *90*(6B), S77–S94. https://0120050077/10.1785/0120000506

Page, R. A., Plafker, G., & Pulpan, H. (1995). Block rotation in east-central Alaska: A framework for evaluating earthquake potential? *Geology*, *23*(7), 629–632. https://0120050077/10.1130/0091-7613(1995)023%3C0629:BRIECA%3E2.3.CO;2

Park, J., & Levin, V. (2016). Anisotropic shear zones revealed by backazimuthal harmonics of teleseismic receiver functions. *Geophysical supplements to the monthly notices of the Royal Astronomical Society*, *207*(2), 1216–1243.

Pavlis, G. L., Bauer, M. A., Elliott, J. L., Koons, P., Pavlis, T. L., Ruppert, N., et al. (2019). A unified three-dimensional model of the lithospheric structure at the subduction corner in southeast Alaska: Summary results from STEEP. *Geosphere*, *15*(2), 382–406. https://0120050077/10.1130/GES01488.1

Plafker, G., & Berg, H. (Eds.) (1994). *The geology of Alaska. Overview of the geology and tectonic evolution of Alaska, The geology of North America series (Vol. G-1, pp. 989–1021)*. America: Geological Society.

Plafker, G., Nokleberg, W. J., & Lull, J. S. (1989). Bedrock geology and tectonic evolution of the Wrangellia, Peninsular, and Chugach terranes along the Trans-Alaska Crustal Transect in the Chugach Mountains and southern Copper River Basin, Alaska. *Journal of Geophysical Research*, *94*(B4), 4255–4295. https://0120050077/10.1029/JB094iB04p04255

Preece, S. J., & Hart, W. K. (2004). Geochemical variations in the <5 Ma Wrangell Volcanic Field, Alaska: Implications for the magmatic and tectonic development of a complex continental arc system. *Tectonophysics*, *392*(1–4), 165–191. https://0120050077/10.1016/j.tecto.2004.04.011

Redfield, T. F., & Fitzgerald, P. G. (1993). Denali Fault System of southern Alaska: An interior strike-slip structure responding to dextral and sinistral shear coupling. *Tectonics*, *12*(5), 1195–1208. https://0120050077/10.1029/93TC00674

Richter, D. H., Smith, J. G., Lanphere, M. A., Dalrymple, G. B., Reed, B. L., & Shew, N. (1990). Age progression of volcanism, Wrangell volcanic field, Alaska. *Bulletin of Volcanology*, *53*(1), 29–44. https://0120050077/10.1007/BF00680318

Ridgway, K. D., Trop, J. M., & Finzel, E. S. (2011). *Modification of continental forearc basins by flat-slab subduction processes: A case study from southern Alaska* (pp. 327–346). Recent Advances: Tectonics of Sedimentary Basins. https://0120050077/10.1002/9781444347166.ch16

Rossi, G., Abers, G. A., Rondenay, S., & Christensen, D. H. (2006). Unusual mantle Poisson's ratio, subduction, and crustal structure in Central Alaska. *Journal of Geophysical Research*, *111*, B09311. https://0120050077/10.1029/2005JB003956

Roy, C., & Romanowicz, B. A. (2017). On the implications of a priori constraints in transdimensional Bayesian inversion for continental lithospheric layering. *Journal of Geophysical Research: Solid Earth*, *122*, 10,118–10,131. https://0120050077/10.1002/2017JB014968

Saltus, R. W., & Bird, K. J. (2003). *Digital depth horizon compilations of the Alaskan North Slope and adjacent Arctic regions*, *U.S. Geological Survey Open-File Report (03-230)*. http://pubs.usgs.gov/of/2003/ofr-03-230/

Saltus, R. W., Potter, C. J., & Phillips, J. D. (2006). Crustal insights from gravity and aeromagnetic analysis: Central North Slope, Alaska. *AAPG Bulletin*, *90*(10), 1495–1517. https://0120050077/10.1306/05090605066

Schulte-Pelkum, V., & Mahan, K. H. (2014a). A method for mapping crustal deformation and anisotropy with receiver functions and first results from USArray. *Earth and Planetary Science Letters*, *402*, 221–233.

Schulte-Pelkum, V., & Mahan, K. H. (2014b). Imaging faults and shear zones using receiver functions. *Pure and Applied Geophysics*, *171*(11), 2967–2991. https://0120050077/10.1007/s00024-014-0853-4

Schulte-Pelkum, V., Mahan, K. H., Shen, W., & Stachnik, J. C. (2017). The distribution and composition of high-velocity lower crust across the continental US: Comparison of seismic and xenolith data and implications for lithospheric dynamics and history. *Tectonics*, *36*, 1455–1496. https://0120050077/10.1002/2017TC004480

Schultz, R. A., & Aydin, A. (1990). Formation of interior basins associated with curved faults in Alaska. *Tectonics*, *9*(6), 1387–1407. https://0120050077/10.1029/TC009i006p01387

Shapiro, N. M., & Ritzwoller, M. H. (2002). Monte-Carlo inversion for a global shear-velocity model of the crust and upper mantle. *Geophysical Journal International*, *151*, 88–105.

Shellenbaum, D. P., Gregersen, L. S., & Delaney, P. R. (2010). Top Mesozoic unconformity depth map of the Cook Inlet basin, Alaska. Alaska Division of Geological & Geophysical Surveys Report of Investigation (2010-2), 1 sheet, scale 1:500,000.

Shen, W., & Ritzwoller, M. H. (2016). Crustal and uppermost mantle structure beneath the United States. *Journal of Geophysical Research: Solid Earth*, *121*, 4306–4342. https://0120050077/10.1002/2016JB012887

Shen, W., Ritzwoller, M. H., Schulte-Pelkum, V., & Lin, F. C. (2012). Joint inversion of surface wave dispersion and receiver functions: A Bayesian Monte-Carlo approach. *Geophysical Journal International*, *192*(2), 807–836. https://0120050077/10.1093/gji/ggs050

Stachnik, J. C., Abers, G. A., & Christensen, D. H. (2004). Seismic attenuation and mantle wedge temperatures in the Alaska subduction zone. *Journal of Geophysical Research*, *109*, B10304. https://0120050077/10.1029/2004JB003018

Tanimoto, T., & Rivera, L. (2008). The ZH ratio method for long-period seismic data: Sensitivity kernels and observational techniques. *Geophysical Journal International*, *172*(1), 187–198. https://0120050077/10.1111/j.1365-246X.2007.03609.x

Tape, C., Silwal, V., Ji, C., Keyson, L., West, M. E., & Ruppert, N. (2015). Transtensional tectonics of the Minto Flats fault zone and Nenana basin, central Alaska. *Bulletin of the Seismological Society of America*, *105*(4), 2081–2100. https://0120050077/10.1785/0120150055

Tappen, C. M., Webster, J. D., Mandeville, C. W., & Roderick, D. (2009). Petrology and geochemistry of ca. 2100–1000 aBP magmas of Augustine volcano, Alaska, based on analysis of prehistoric pumiceous tephra. *Journal of Volcanology and Geothermal Research*, *183*(1–2), 42–62. https://0120050077/10.1016/j.jvolgeores.2009.03.007

Till, A. B. (2016). A synthesis of Jurassic and Early Cretaceous crustal evolution along the southern margin of the Arctic Alaska–Chukotka microplate and implications for defining tectonic boundaries active during opening of Arctic Ocean basins. *Lithosphere*, *8*(3), 219–237. https://0120050077/10.1130/L471.1

Till, A. B., Dumoulin, J. A., Phillips, J. D., Stanley, R. G., & Crews, J. M. (2006). Generalized bedrock geologic map, Yukon Flats region, east-central Alaska. *U.S. Geological Survey Open-File Report*, *1304*(1).

Trop, J. M., Hart, W. K., Snyder, D., & Idleman, B. (2012). Miocene basin development and volcanism along a strike-slip to flat-slab subduction transition: Stratigraphy, geochemistry, and geochronology of the central Wrangell volcanic belt, Yakutat–North America collision zone. *Geosphere*, *8*(4), 805–834. https://0120050077/10.1130/GES00762.1

Trop, J. M., & Ridgway, K. D. (2007). Mesozoic and Cenozoic tectonic growth of southern Alaska: A sedimentary basin perspective. In K. D. Ridgway, J. M. Trop, J. M. G. Glen, & J. M. O'Neil (Eds.), *Tectonic growth of a collisional continental margin: Crustal evolution of south-central Alaska* (Vol. 2431, pp. 55–94). America: Geological Society.

Van Kooten, G. K., Richter, M., & Zippi, P. A. (2012). Alaska's Interior rift basins: A new frontier for discovery. *Oil and Gas Journal, Exploration and Development.*. https://0120050077/10.1139/cjes-2015-0138

Vidale, J. E., & Helmberger, D. V. (1988). Elastic finite-difference modeling of the 1971 San Fernando, California earthquake. *Bulletin of the Seismological Society of America*, *78*(1), 122–141.

Vinnik, L. P. (1977). Detection of waves converted from P to SV in the mantle. *Physics of the Earth and Planetary Interiors*, *15*(1), 39–45. https://0120050077/10.1016/0031-9201(77)90008-5

Wang, M., Hubbard, J., Plesch, A., Shaw, J. H., & Wang, L. (2016). Three-dimensional seismic velocity structure in the Sichuan basin, China. *Journal of Geophysical Research: Solid Earth*, *121*, 1007–1022. https://0120050077/10.1002/2015JB012644

Wang, Y., & Tape, C. (2014). Seismic velocity structure and anisotropy of the Alaska subduction zone based on surface wave tomography. *Journal of Geophysical Research: Solid Earth*, *119*, 8845–8865. https://0120050077/10.1002/2014JB011438

Ward, K. M. (2015). Ambient noise tomography across the southern Alaskan cordillera. *Geophysical Research Letters*, *42*, 3218–3227. https://0120050077/10.1002/2015GL063613

Ward, K. M., & Lin, F. C. (2018). Lithospheric structure across the Alaskan cordillera from the joint inversion of surface waves and receiver functions. *Journal of Geophysical Research: Solid Earth*, *123*(10), 8780–8797. https://0120050077/10.1029/2018JB015967

Ward, K. M., Zandt, G., Beck, S. L., Christensen, D. H., & McFarlin, H. (2014). Seismic imaging of the magmatic underpinnings beneath the Altiplano-Puna volcanic complex from the joint inversion of surface wave dispersion and receiver functions. *Earth and Planetary Science Letters*, *404*, 43–53. https://0120050077/10.1016/j.epsl.2014.07.022

Wilson, F. H., Hults, C. P., Mull, C. G., & Karl, S. M., comps (2015). Geologic map of Alaska: U.S. Geological Survey Scientific Investigations Map 3340, 197 p., 2 sheets, scale 1:584,000. https://0120050077/10.3133/sim3340

Yeck, W. L., Sheehan, A. F., & Schulte-Pelkum, V. (2013). Sequential H-κ stacking to obtain accurate crustal thicknesses beneath sedimentary basins. *Bulletin of the Seismological Society of America*, *103*(3), 2142–2150.

Zhang, Y., Li, A., & Hu, H. (2019). Crustal structure in Alaska from receiver function analysis. *Geophysical Research Letters*, *46*, 1284–1292. https://0120050077/10.1029/2018GL081011